

BRIDGE-RIDGE-STRAINED PLASMA: COLLIER/Quinn (2019)

by

JOHN RAY JAMES

A DISSERTATION PRESENTED TO THE GRADUATE SCHOOL
OF THE UNIVERSITY OF FLORIDA
IN PARTIAL FULFILLMENT OF THE REQUIREMENTS
FOR THE DEGREE OF DOCTOR OF PHILOSOPHY

UNIVERSITY OF FLORIDA

2019

DEDICATED TO MY LATE FATHER

ACKNOWLEDGMENTS

First of all, I would like to express my deep gratitude to my advisor Dr. Rana V. Amamany for his guidance, support, and encouragement. His leadership is directly responsible for the completion of this work without any interruption.

Several other professors provided valuable advancement and assistance. I would like to thank Dr. Ranaam Delivians for useful discussions and the well-organized operation of the Photonics Research Laboratory. He also served as my supervisory committee. I am grateful to Dr. Peter Sory who, in addition to service as my supervisory committee, provided advancement and discussions, especially about LIP growth, cleaning, and device characterization. He also allowed me to use the characterization facility in his research laboratory. I am deeply indebted to Dr. Luis Figueroa of the Texas High Technology Electronics Center who had been my advisor for two years. His enthusiasm stimulated my first interest in semiconductor lasers. He also taught me how to use the LIP machine, provided LIP information, characterized some of my devices, and reviewed my dissertation. I also thank Dr. Wang X. Li and Dr. Mark Green for serving as my supervisory committee.

I have to recognize other individuals who have provided invaluable assistance. I wish to thank James Chastine and Jim

roles of the Microelectronic Laboratory for all the technical assistance they provided over the years; I also thank Allan Bartberger for machining of certain components used in my experimental set-ups, and Bob Search for his help in fixing the mass flow controller.

I wish to thank my fellow graduate students, Xinyi-Chiao Chang, Young Isaac Kim, Sam Sun Lee, Bao Jinchun, Erik Lewis, Chris Russell, Jessica Wilson, and Janet Weiner for useful discussions. In addition, I thank Dr. Rongguo Jiaoy and Dr. Young June Yu whose friendship made my stay at the University of Florida much more enjoyable.

Lastly, but not the least, I thank my wife Chany Wan and my daughter Jane Yang for their understanding and love. I also thank my parents, my brothers, and my wife's parents for their encouragement and support.

TABLE OF CONTENTS

	Page
ACKNOWLEDGMENTS	181
ABSTRACT	181
CHAPTER	
ONE INTRODUCTION	1
TWO LIQUID PHASE EPITAXY (LPE)	13
2.1 Basic Principles of Liquid Phase Epitaxy	13
2.2 Procedures for Liquid Phase Epitaxy	18
2.3 Material Preparation	20
2.4 Typical problems in LPE	21
THREE SOLID-SOLID-STRIPPED FLAMES	
GROWTH STRUCTURE CATALOG	25
3.1 INTRODUCTION	25
3.2 Well-Ordered Lower Stripes Structures	28
3.2.1 Double Misorientation Growth	28
3.2.2 Ridge Formation	30
3.2.3 Preferential Growth	30
3.2.4 Preferential Melt-Stop	32
3.2.5 Growth on Melt-Exposed Channel	32
3.3 Solid-Ridge Striped Flamer Structure	33
3.3.1 Simultaneous Preferential Growth and Preferential Melt-Stop	34
3.3.2 Preferential Melt-Stop in Equilibrium Solution Followed by Preferential Growth	39
3.3.3 Preferential Melt-Stop in Undersaturated Solution Followed by Preferential Growth	41
3.3.4 Preferential Growth Followed by Preferential Melt-Stop in Undersaturated Solution	44
3.4 Fabrication Procedure of Striped-Solid-Stripped Flamer Structure	45
3.4.1 First Step LPE Growth	45
3.4.2 Ridge Formation	50
3.4.3 Second Step LPE Growth	51
3.4.4 W-Type Gratic Contour	55
3.4.5 Tapping	55
3.4.6 I-Type Gratic Contour	55
3.4.7 Sliding	56
3.4.8 Clipping	56

FOUR	COMPLEX DOMAIN EFFECTIVE INDEX METHOD.....	57
	4.1. Introduction.....	57
	4.2. Complex Domain Characteristic Equations.....	59
	4.3. Miller Method.....	61
	4.4. Branch Specifications in the Periodic Layers.....	65
	4.5. Piecewise Uniform Approximation of Transverse Effective Index Profile.....	75
	4.6. Mode Calculations.....	78
	4.7. Structural Loss Estimation.....	82
	4.8. Summary and Conclusion.....	83
FIVE	ANALYSIS OF THE BOUNDED-WIDTH-STRIPED PLASMA STRUCTURE.....	90
	5.1. Introduction.....	91
	5.2. Mode Analysis.....	91
	5.3. Effective Index Approach.....	93
	5.4. Experimental Results.....	95
	5.5. Discussion.....	98
SIX	SEPARATED LARGE OPTICAL CAVITY LAYERS.....	122
	6.1. Introduction.....	122
	6.2. Mode Analysis.....	125
	6.3. Experiments.....	128
	6.4. Self-Coupled Normal Modes.....	129
	6.5. Conclusion.....	132
SEVEN	SUMMARY AND RECOMMENDATIONS.....	134
	7.1. Summary.....	134
	7.2. Recommendation for Further Study.....	139
REFERENCE	142
BIOGRAPHICAL SKETCH	148

Abstract of Dissertation Presented to the Graduate School
of the University of Florida in Partial Fulfillment of the
Requirements for the Degree of Doctor of Philosophy

MODIFIED-BLOCK-STRIPED PLANAR GaAlAs/GaAs LADERS

By

ROSE ANN LEE

May 1996

Chairman: PAUL Y. KUMARASEKAR

Major Department: Electrical Engineering

First, a novel modified-block-striped planar (MBSP) GaAlAs/GaAs lader is proposed, analyzed, fabricated, and tested. The MBSP structure is grown by a two-step liquid phase epitaxy (LPE) scheme using preferential growth and preferential etch-back techniques. In the MBSP structure, a double heterostructure is grown above an inner stripe which is formed by preferential growth of a $x\text{-Ga}_{1-y}\text{Al}_y\text{As}$ current blocking layer outside a $y\text{-Ga}_{1-x}\text{Al}_x\text{As}$ ridge and by preferential etch-back of the thin GaAs layer on top of the ridge. The Al mole fraction y in the $x\text{-Ga}_{1-y}\text{Al}_y\text{As}$ current blocking layer can be widely varied by > 0.051 from the Al mole fraction x in the $y\text{-Ga}_{1-x}\text{Al}_x\text{As}$ buried-ridge. Thus, the MBSP structure can incorporate various kinds of effective index steps, e.g., positive, negative, and complex index steps.

To analyze the BHP structure, the conventional real-domain effective index method is extended into the complex domain. The analysis at threshold shows that, in both positive and negative step structure, the imaginary part of the effective index exhibits a relatively small step between the stripe and outside region. However, in complex step structures, the imaginary part of the effective index shows a large step and is hardly affected by the gain induced refractive index change Δn_g . As a result, in this case, the lateral mode is very stable. The measured threshold current and the external differential efficiency of the BHP structure were $I_0 = 100$ mA and $\eta = 25\%$, respectively. As expected, two-lobed far field patterns were obtained in the negative step structure while single-lobed far field patterns were observed in both the positive and the complex step structures.

Second, a novel separated large optical cavity (SLOC) scheme was proposed and demonstrated. The coupling between optical modes of the composite structure consisting of the active guide and the SLOC guide, under gain conditions, increases the effective transverse mode size. As a result, the maximum available output power of the SLQ structure is about twice that of the standard non-SLOC structure, although the threshold is higher.

CHAPTER ONE INTRODUCTION

Since semiconductor-wave (CW) operation of the GaAs/GaAlAs semiconductor laser was realized at room temperature in 1970 [Kaye70, Hayaki], the research emphasis has been to develop wide laser structures capable of controlling the modal behavior in spatial domains [Kaye70]. The mode stabilization in the transverse direction can easily be achieved by reducing the active layer thickness. The thinner active layer also provides other benefits, such as reduced threshold current and increased transverse mode size. The mode may also be stabilized in the lateral direction by similarly reducing the lateral dimension of the device (the current injection stripe). However, the available output power would be severely limited with a very narrow stripe.

High power lasers invariably use larger stripe widths resulting in larger mode values. However, in this case, the modes often become unstable. Therefore, for better stabilization with reasonably wide stripes, it will be useful to incorporate an optical guiding mechanism in the lateral direction, the so-called the built-in effective index step. Conventionally two types of effective index steps, i.e., the positive step [Salt88] and the dispersive step [Muro89] have been investigated in detail. The effective index configuration shown in Figure 1.1 is called the positive



$$N_I > N_{II}$$

Figure 1.1. A positive effective index step structure. The effective index in region I, N_I , is larger than the effective index in region II, N_{II} .

effective index step since the effective index in the stripe region is higher than that outside the stripe. In general, a mode tends to propagate in the region of higher effective index. Thus, in the positive index step structure, the mode is stabilized inside the stripe region. On the other hand, in the complex effective index step structure shown in Figure 1-2, the mode index (effective index) outside the stripe has a complex number with a large imaginary part (large mode loss). As a result, in a complex effective index step structure, the mode tends to be stabilized inside the stripe, since the mode experiences significantly larger loss outside the stripe. Recently, however, another type of effective index step known as the negative step has received considerable attention due to its excellent performance in linear arrays. Figure 1-3 shows the effective index configuration for the negative step [Rajiv] in which the effective index in the stripe region is smaller than that outside the stripe. Both the negative and the complex step structures are very lossy. However, by compensating the structure loss with gain, guiding can be achieved even in these structures.

It is well known that the negative effective index step provides very strong lateral coupling between elements, leading to a very stable array mode operation (Goodall, Hewlett, Kuroki). Conventional linear array lasers which utilize mostly the complex effective index step (Rataki) are not quite useful since significant substrate radiation loss



$$N_I \quad N_{II}^*$$

Figure 1.2 A complex effective index step structure. The effective index in region II, N_{II}^* , is a complex number with a large imaginary part.



$$N_I < N_{II}$$

Figure 1.12 A negative effective index step structure. The effective index in region I, N_I , is smaller than the effective index in region II, N_{II} .

between elements minimizes the lateral coupling effect as shown schematically in Figure 1-4.

The main objective of this dissertation is to develop a new GaAs/GaAlAs diode laser geometry capable of controlling the effective index with sufficient flexibility. Not many diode laser geometries developed so far, can incorporate the various kinds of effective index steps, e.g., positive, negative, and complex index steps. For example, only the positive effective index step is available in the ridge waveguide structure [Reda77], and the channelled substrate planar structure [Hart80] incorporates only the complex effective index step. One exception is the buried heterostructure in which the effective index step can easily be controlled over a wide range by varying the refracting index of the burying layer [Kaji72]. However, the buried heterostructure is not quite useful for linear array applications. The strong lateral coupling between elements is not available in a linear array laser using a negative step (anti-guide or leaky-guide) buried heterostructure [Kishi81], since the diffraction loss would be very high between elements with no optical guide mechanism, as shown schematically in Figure 1-5.

This dissertation describes the development, in particular, of a novel GaAs/GaAlAs diode laser geometry namely the buried-ridge etched planar (BREP) structure and the separated large optical cavity (SLOC) structure. The BREP structure is grown by a novel two-step liquid phase epitaxy

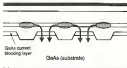


Figure 1.4 Schematic diagram of the DBT type linear array laser.

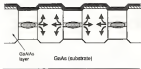


Figure 1-5 Schematic diagram of the leaky mode coupled RA type linear array laser

ILDP) allows using preferential growth and self-align techniques, and incorporates the various effective index steps, described above, in a configuration with a continuous active layer.

In order to analyze the HMP structure, the conventional effective index method was extended into the complex domain. A structure (Fig. 2), the HMP structure involving modes with complex propagation constants in any of the distinctive regions either along the transverse or the lateral direction, cannot be analyzed, in general, by using the conventional real domain effective index method. The complex domain effective index method retains the simplicity of the conventional effective index method. In the effective index method, a complicated two-dimensional problem is easily handled as two one-dimensional problems.

The side control in the transverse direction is also very important; the schemes to control the transverse mode, i.e., the thin active layer (TAL) scheme and the large optical cavity (LOC) scheme have been extensively investigated, mainly to increase the transverse mode size and hence increase maximum available output power. In the conventional LOC scheme, the LOC layer with a relatively smaller bandgap is in direct contact with the active layer. Thus, as a result of the decreased bandgap difference between the active layer and the LOC layer, the active layer carrier confinement may become poor especially at high injection level. However, in the separated large optical cavity (SLOC)

where, a thin layer with a smaller bandgap separates the LOC layer and the active layer providing enough barrier for the injected carriers in the active layer.

Even though the LOC layer and the active layer are physically separated from each other, they are optically connected as a result of the overlap of the active guide mode and LOC guide mode. The normal modes are no longer orthogonal under a condition of the coupled refractive index due to either the active layer gain or loss in the layers. Coupling is shown to occur under gain between the active guide mode and the LOC guide mode. This mode coupling has the effect of increasing the transverse mode size and hence the maximum available output power. To the best of our knowledge this is the first time such a mode coupling is demonstrated.

The organization of the dissertation is as follows: Following the introduction in chapter one, the basics of the liquid phase epitaxy are described in chapter two. In chapter three, the novel liquid phase epitaxy growth scheme used to fabricate the DBF structure is explained in detail. In chapter four, the coupled domain effective index method is developed by extending the conventional real domain effective index method into the complex domain. In chapter five, the DBF structure analysis and the experimental results are presented. In chapter six, a novel separated large optical cavity (SLOC) scheme to increase the effective transverse mode size and hence increased power output is demonstrated.

The EDC lens performance is compared with that of non-EDC, i.e., conventional DE lenses. Finally, in chapter seven, the results are summarized and recommendations for further study are presented.

CHAPTER TWO

LIQUID PHASE EPITAXY (LPE)

Liquid phase epitaxy (LPE) (Kraus¹, Hata²) is one of the oldest techniques used to grow GaAs/AlGaAs epitaxial layers. It continues to be an important technique, even today, especially for the fabrication of laser and light emitting diodes. Some of the advantages of the LPE over either the molecular beam epitaxy (MBE) or the metal organic chemical vapor deposition (MOCVD) are as follows. (i) the LPE technique is well established, (ii) it produces relatively good quality film, (iii) the LPE system and the maintenance are relatively inexpensive, and (iv) various device geometries can be grown using either preferential growth or multi-step depending on topography of the substrate. However, LPE technique has certain significant disadvantages compared to either MBE or MOCVD technology. For example, it is hard to grow very thin layers, and in general, the uniformity of the layers is relatively poor. Furthermore, growth on a GaAs layer whose Al mole fraction is larger than 0.1 can hardly be achieved (Hata³).

2.1: Basic Principles of Liquid Phase Epitaxy (LPE)

Liquid phase epitaxial growth, basically, involves the precipitation of a material from a supersaturated solution on to a underlying substrate. For example, the equilibrium

concentration of Al in Ga solution depends on the temperature as shown in Figure 2.1. Thus, if the temperature of the equilibrium solution is being lowered, the solution becomes supersaturated and material, in this case, Ga, precipitates.

A simplified block diagram of the LPE system is shown in Figure 2.2. The growth occurs in a pyrolytic graphite boat inside quartz tube in a highly purified H_2 environment. The water-cooled horizontal sliding boat, schematically shown in Figure 2.2, is commonly used since it allows sequential growth of multilayers.

A typical growth temperature program is shown in Figure 2.4. The main reason for preheating of Ga is the reduction of Ga oxide which otherwise upon decomposition would cause the oxidation of the Al component (Botske). The Al oxide is undesirable, as it is not reduced at usual growth temperatures ($T_{90} = 850^\circ C$). The Ga preheating may not be necessary, if pure Ga ingots are used instead of liquid Ga (liquid Ga is readily oxidized). After preheating Ga and evaporative deposits (Ga, Ga₂), the cleaned substrate as well as Ga₂ and Ga₃ crystal, Al, and volatile (Ga, Ga₂) are loaded into appropriate bins, as shown in Figure 2.3. Then the temperature is raised to $T_1 (= 800^\circ C)$ and is homogenized for 2 - 3 hours so that the melt reaches an equilibrium. After homogenization, the system is cooled down by an amount $\Delta T (= 5^\circ C)$ at a rate of about 2-3 $^\circ C/min$. The substrate is then slid underneath the first melt and is kept there for an appropriate time to grow an epitaxial layer with a desired

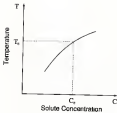
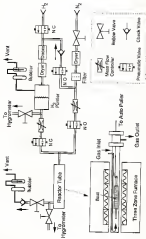


Figure B.1. At temperature T_m , solid GaAs is in equilibrium with Ga liquid of Ga concentration C_m .



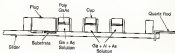


Figure 2-5 A simplified schematic diagram of a graphite line.



Figure 2.4 A temperature program for LPE growth. Typical numbers for growth parameters are: $T_h = 600^\circ\text{C}$, $T_c = 500^\circ\text{C}$, $\Delta T = 5^\circ\text{C}$, $S = 0.5^\circ\text{C/min}$.

thickness. The substrate is then slid underneath the adjacent wafer sequentially for the growth of the next layers.

In our LPE system, an vacuum pump is installed, and the pure H_2 environment inside the reactor can be achieved only by flowing H_2 for significant amount of time. It is very important to achieve the pure H_2 environment as quickly as possible in order to minimize the oxidation of loaded materials. Detailed growth procedure is described in the following section.

2.2- Experiment for Liquid Phase Epitaxy

Ga loading

After the boat is carefully wiped with lint-free paper, each well to be used is loaded with 2.2 gm Ga. Carefully weighed semiconductor deposits, such as Ga (p-type), and In (n-type), are also loaded at the same time. It is noted that, in order to minimize oxygen flow into the reactor during time the reactor is opened to air, H_2 gas should be flowing inside the reactor at a very high rate (about 33 cc/min).

Reactor Flushing

Since the reactor was opened for Ga loading, the reactor should be flushed by flowing H_2 . The minimum flushing time for reasonably pure H_2 environment is about 3 hours at a flow rate of 33 cc/min.

Preheating

Ga is heated at temperature of 800 °C for 5 ~ 10 hours. During the heating, the H_2 flow rate is reduced to 3 cc/min.

Substrate Loading

The preheating is finished by removing the furnace, which is on a sliding rail, away from the reactor tube. During the time the reactor is being cooled down to room temperature, the substrate and weighed source materials, such as GaAs, poly crystal, Al, and volatile deposits (Fe, Sn) are being prepared for loading. It is important to load these materials quickly to minimize the oxidation.

Reactor Flushing

The reactor is flushed once again with H_2 by following the same procedure as in the previous step.

Isospeedization

The system is isospeedized at temperature of about 800 °C for 5 ~ 10 hours so that the mix reaches an equilibrium. During the isospeedization, the H_2 flow rate is kept to 3 cc/min.

Exposure and Growth

The system is cooled down at a rate of about 2.5 °C/min. When the temperature drop ΔT is about 1 °C, the growth is

initiated by sliding the substrate under the supercooled melt.

Sample Removal and Post-Cleanups

The furnace is moved away from the reactor tube the growth is completed. After the grown sample is taken out, the boat is carefully wiped of Ga melt with lint-free paper for the next run. The next run may start at this point by loading the Ga. If not used for a while, the reactor is cleaned and flushed by flowing H_2 at a rate of about 1 - 2 cc/min.

3.3 Material Preparation

In liquid phase epitaxy, the material preparation is very important and is described in this section.

Substrate:

Dip Ga wire TCE for 10 min;

Rinse in acetone;

Rinse in methanol.

Rinse in deionized (DI) water;

Etch in $HNO_3 + H_2O_2 + H_2O = 28 : 7 : 100$ solution

for 1 - 2 min;

Rinse in DI water

Thin crystal disk:

Etch in $H_2SO_4 + H_2O_2 + H_2O = 1 : 1$ solution for 1 min;

Rinse Ga DI water.

Suspension

Etch in HCl solution for 5 min

Rinse in DI water

In order to minimize the exposure to air, the above etched materials should be kept in oil water until the final rinse before loading. The materials are then dried by blowing H_2 immediately before loading.

2.4. Typical Etching in HCl

The graphite boat should always be kept clean, since the actual growth takes place inside the boat. However, as the number of runs with one boat increases, the growth quality becomes deteriorated due to contamination. The important contaminants are Al, Fe, and Zn which are easily oxidized (log ϕ 78). The surface of the samples grown under the condition of serious oxidation are usually not very shiny, because of a relatively high density of the defects as shown in Figure 2.3(a). Similar results were often obtained when the reactor flushing is not appropriate. For example, the reactor flushing with lower H_2 flow rate for longer time is not as good as the flushing with higher H_2 flow rate for shorter time, since more oxidation occurs by the residual O_2 during the longer flushing time.

In order to minimize the contamination, the best should be checked regularly. One of the simple procedures is to take



(a)



(b)

Figure 8. Typical problems in IPE
 (a) Sample grown under oxidized condition,
 (b) Overgrowth due to salt-carry over.

either the bare boat or the boat filled with Sn under vacuum. It is far several hours at higher temperature (900 °C) than the growth temperature [Betz94]. In this case, it is important not to raise the temperature very high, since the devitrification of quartz tube becomes a serious problem at higher temperatures.

Another very common problem is LFE in the melt carry-over on the grown sample. The melt carry-over usually occurs when the substrate is sold out of the boat melt, because of the pressure difference between the well with a melt and the empty well. An example is a sample shown in Figure 2-100. The top layer is very thick due to the very rapid growth from the carry-over melt during the rapid cooling process. It is important to reduce the melt carry-over, since the very thick layer grows with a melt carry-over usually prevents further processing. A small amount of the melt carry-over usually occurs between the growth of the lower layers and the growth of the previous layer continues in the next well. This may be one of the reasons for the relatively poor thickness controllability of the liquid phase epitaxy. The melt carry-over to some extent, is directly related to the boat design. We have also found that n-type dopants such as Te and Se reduce the melt carry-over significantly, while the p-type dopants such as Ge and Sn increase the melt carry-over. Thus, it may be useful to grow a thin initial n-type Se-doped layer, as the last layer, to reduce melt

copy-over and the extra o-type data layer may be removed later by etching.

CHAPTER THREE

GROWTH OF THE INDEX-RISE-STRIPED PLASMA STRUCTURE

3.1 Introduction

One of the unique features of the liquid phase epitaxy (LPE) is that the growth rate [Figs79] is strongly dependent on the topography of the substrate. As seen in the liquidus curve shown in Figure 1.1, the equilibrium A_0 concentration has lower value on the concave surface than on the convex surface. As a result, a melt of concentration C_0 at temperature T_0 is effectively undersaturated for the convex surface and is effectively supersaturated for the concave surface. Thus, there is always tendency to fill in concave parts of the surface and melt-rich convex parts of the surface. The preference of LPE growth for concave surface over convex surface is a very important factor in the shaping of the various groove layers in the structures, such as the channelled substrate planar (CMP) structure [Fure79], buried heterostructure (BH) [Leit81], and the restricted double heterostructure (RDHP) [Nata81].

One of the problems with the LPE technique is that a reproach can be made only either on a GaAs or a $\text{Ga}_{1-x}\text{Al}_x\text{As}$ layer with relatively lower Al mole fraction $x < 0.1$ [Frank81]. This reproach problem seriously limits the use of LPE technique to grow various device geometries. For example,

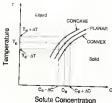


Figure 3.1 Liquidus curves for planar, concave, and convex surfaces across the temperature T_0 . At T_0 , a solid of planar surface is in equilibrium with a liquid of solute concentration C_0 .

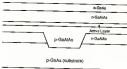


Figure 3.3 The conventional LPE scheme may not be used to fabricate the above structure, due to a serious problem in depositing an GaAs layer.

the geometry shown in Figure 3-2 which can incorporate various types of effective index steps (by varying the current blocking layer Al concentration) cannot be grown by the conventional LPE growth scheme. However, researchers at GRI company overcome this problem by developing a novel LPE scheme. This method combines the preformal growth and wet-etch, thus eliminating the regrowth problem in the fabrication of the wet-etched laser stripe (WELS) structure [Kato85]. However, one problem of the WELS structure is that the controllability of the built-in effective index step is very much limited as in the conventional QW structure.

However, in the buried-ridge-etched planar (BREPP) structure presented in this dissertation, the growth procedure has been modified to incorporate the various effective index steps, such as the positive, the negative, and the complex step. In this chapter, the detailed fabrication procedure of the BREPP structure [Lee88a] is described.

3.3 Buried-Ridge-etched Laser Stripe (BREPP) Structure

In this section, the fabrication procedure of the wet-etched laser stripe (WELS) structure is briefly reviewed. This review will help understand the fabrication procedure of the BREPP structure. Each growth step of the WELS structure is shown in Figure 3-3 and is described below:

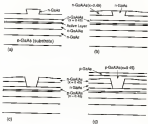


Figure 3.2 The growth procedure of the salt-stained laser stripe DBR structure:
 (a) First step growth and edge formation,
 (b) Preferential growth of mid-edge mask,
 (c) Preferential mid-edge of n-GaAs layer,
 (d) Growth of p-type cladding and contact layers.

3.3.1 Double Heterostructure Growth

A double heterostructure with a relatively thin (3 μm) p-type upper cladding layer and a very thick (3 μm) n-type GaAs layer on top is grown on a n-type substrate. In the subsequent steps, an inner stripe will be formed in the thick GaAs layer.

3.3.1.1 Ridge Formation

As the first step to make an inner stripe, a reversed ridge is formed in the top GaAs layer along the $\langle 110 \rangle$ direction by chemical etching as shown in Figure 3.3(a). In the ridge forming process, no GaAs layer is exposed to air, and thus, the regrowth problem doesn't exist.

3.3.1.2 Preferential Growth

In the second step growth, first a $\text{Ga}_{1-y}\text{Al}_y\text{As}$ ($y > 0.45$) layer is preferentially grown outside the ridge as shown in Figure 3.3(b). The growth rate over the ridge region with convex topography is very small or negative (self-etch) compared to that in the region outside the ridge. The preferentially grown $\text{Ga}_{1-y}\text{Al}_y\text{As}$ ($y > 0.45$) layer should be an effective self-etch mask in the next self-etch step.

3.3.1.3 Preferential Self-Etch

After the preferential growth of the $\text{Ga}_{1-y}\text{Al}_y\text{As}$ layer, the substrate is moved under an undifferentiated solution (by

about 3°C is sufficient to buried GaAs ridge as shown in Figure 3.10(c). The $\text{Ga}_{1-x}\text{Al}_x\text{As}$ ($x = 0.35$) layer is hardly self-aligned and acts as an effective self-align mask, since the self-align rate decreases as the Al mole fraction x increases. Therefore, in the underetched well, the buried GaAs ridge will be preferentially self-aligned. Then, a complete channel shown in Figure 3.10(c) will be formed as the self-align stops on the p-GaAs upper cladding layer which is also hardly self-aligned. In the MBE structure, a large self-align selectivity between the GaAs ridge and the self-align mask is required and the Al mole fraction of the $\text{Ga}_{1-x}\text{Al}_x\text{As}$ self-align mask should be relatively large ($x \geq 0.4$). The reasons for that are: 1) the GaAs layer to be self-aligned is very thick (3 μm), and 2) large underetching of the well is needed to self-align into a channel, because the effective underetching becomes smaller inside the channel due to increased conductivity.

3.1.3 Growth on Self-Aligned Channel

As the final step, the self-aligned channel is filled in by growing a GaAs cladding layer and a GaAs contact layer as shown in Figure 3.10(d).

3.2 Buried-Ridge Striped-Barrier (BRSB) Structures

In the MBE structure, an InAs stripe is formed during the second step LPE and is located above the double

interconnections which is given in the flow step IPE. In this configuration, only a large 8λ wide GaAs buffer layer can be used as an integral anti-etch mask as explained in the previous section and the selectivity of the etching layer step is very much limited. It is noted that the refractive index of the GaAs anti-etch mask is a very important parameter in determining the effective index step of the structure. This will be discussed in chapter five in more detail.

In the buried-ridge-stripped planar (BRSP) geometry, an inner stripe is formed first before the growth of a double heterostructure. In the BRSP geometry, as the first step to form an inner stripe, either a double etched ridge or a simple ridge shown in Figure 3.4 is formed after the first step growth of three layers: a p -GaAs buffer layer ($1\mu\text{m}$), a p -GaAs_{0.45}Si_{0.55} layer ($1\mu\text{m}$), and an undoped GaAs layer ($1\mu\text{m}$). The cross-sectioned view in Figure 3.4(b) does not correctly show the inner ridge on the left hand side due to an artifact in the way the sample is prepared in the SEM. An inner stripe can be formed by preferentially growing a n -Ga_{0.45}Si_{0.55} current blocking layer outside the ridge and preferentially anti-etching the thin GaAs on top of the ridge.

It is noted that the ridge in the BRSP geometry consists of a GaAs layer and a thin GaAs layer on top, instead of a pure GaAs layer as in the BRP geometry. Only the thin GaAs on top of the ridge should be removed by the anti-etch. In



(a)



(b)



(c)

- Figure 3.4 First λ nm growth and transfer mechanism of the
 HEMT structure
 (a) Double Channel Ridge,
 (b) Single Ridge,
 (c) SEM cross-sectional view of Single Ridge.

condition, in the RHEP structure, the thin (5.3 μ m) GaAs layer to be melt-riched is located on top of the ridge with convex topography where the melt may be effectively undersaturated. Thus, the thin GaAs layer in the RHEP structure is more easily removed compared to the thick buried GaAs ridge in the DHEP structure. Several different schemes to preferentially melt-rich the thin GaAs layer on top of the ridge and to preferentially grow the current blocking layer outside the ridge have been tested. Some of the attempted schemes to achieve this structure are explained in the next sections.

3.3.1: Simultaneous Preferential Growth and Preferential Melt-rich

In the RHEP configuration, the GaAs layer to be melt-riched is located on top of the ridge with convex topography (favored for preferential melt-rich). On the other hand, the area where a current blocking layer is to be grown has a concave topography (favored for preferential growth). A melt with properly adjusted supersaturation may be effectively undersaturated over the ridge while it is effectively supersaturated in the rest of the area. In this case, the preferential growth of the current blocking layer and the melt-rich of the thin GaAs on top of the ridge can be achieved in a single melt. If this scheme works, it would have a significant advantage since a separate undersaturated melt need not be prepared. Both the double channel ridge and

the single ridge configuration shown in Figure 3.4. Such tests tested.

In the case of double channel ridges, if the supersaturation is increased, layers hardly grow on extremely convex areas resulting in the discontinuous current blocking layer and active layer as seen in Figure 3.5. A similar effect is observed in the growth of the double channel pinner based heterostructure (DCPHS) [Schaff], in which the internal burying layers are not grown over the ridge region. On the other hand, if the salt supersaturation is reduced, the grown layers are very irregular as shown in Figure 3.6 and it is very difficult to control the layer thickness. However, in the case of the single ridge configuration, the growth characteristics is much less complicated and the discontinuity of the grown layers is not observed as shown in Figure 3.7.

The most difficult problem of this scheme is that the convexity of the ridge decreases as the growth of the current blocking layer continues. Thus, in most of the cases, the thin GaAs layer on top of the ridge is hardly removed as shown in Figures 3.3, 3.8, and 3.9. Even with a reduced supersaturation of the salt, the thin GaAs layers still remains on top of the ridge as shown in Figure 3.4. In general, large supersaturation is desirable for better preferential growth; however, the increased supersaturation makes the simultaneous preferential salt-etch more difficult.

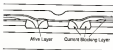


Figure 3-3 Simultaneous preferential growth and preferential melt-back, super cooling $\Delta T = 3^\circ\text{C}$, cooling rate $R = 0.5^\circ\text{C/min}$ (double channel stage)



Figure 1.4 Simultaneous preferential growth and preferential melt-back, super cooling $\Delta T = 4^\circ\text{C}$, cooling rate $S = 0.3^\circ\text{C/min}$ (double channel ridge).



Figure 9. (a) Simultaneous preferential growth and preferential wetting, super cooling $\Delta T = 5$ K; cooling rate $\beta = 0.7$ °C/min (sample stage).

In conclusion, the simultaneous growth and melt-back scheme doesn't seem to work in both the double channel ridge and single ridge configurations, and thus, the growth of the current blocking layer and the melt-back of the thin GaAs layer should be performed separately in two different steps. Another finding is that the single ridge configuration has a clear advantage over the double channel ridge configuration in terms of the grown layer uniformity.

3.3.2 Preferential melt-back in Equilibrium Solution followed by Preferential Growth

In this scheme, first, the sample is immersed in an equilibrium solution with some degree supersaturation for an appropriate time before the supersaturation starts. The equilibrium melt may be effectively under-saturated over the ridge with convex topography and melt-back the thin GaAs layer on top of the ridge. The sample is then moved into a supersaturated melt for the preferential growth of the current blocking layer.

One of the samples grown by this scheme is shown in Figure 3.8. In this scheme, the GaAs layer is melt-backed in general only in the area near the edge of the ridge where the melt is effectively under-saturated due to the large convexity. The effective supersaturation in the region away from the edge of the ridge may be too small to melt-back the GaAs layer completely. In conclusion, the topographical

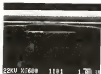


Figure 1.8. Preferential meltback of oxide layer in equilibrium solution followed by preferential growth of the current bleeding layer, under superheat $\Delta T_s = 5.0^\circ\text{C}$ (melt-back), melt-back time $t_m = 10$ sec, superheat $\Delta T_s = 5.0^\circ\text{C}$ (growth), cooling rate $\dot{S} = 0.7^\circ\text{C/min}$.

correctly since the ridge is not sufficient to with-stand the thin GaAs layer by an equilibrium melt.

3.3.3 Preferential melt-stick in Undersaturated Solution Followed by Preferential Growth

In this scheme, a saturated melt with undersaturation is prepared in the first well of the boat using the temperature program shown in Figure 3.3. At the end of the preheating, the system temperature is lowered to T_{sat} . After the temperature is stabilized, a piece of polycrystalline GaAs is added underneath the first Ga melt to make an equilibrium solution at temperature T_{sat} . The remaining GaAs polycrystal should be removed from the melt before the furnace is moved away from the reactor. In the homogenization process, the temperature T_h should be properly adjusted so that the first melt temperature reaches T_h after cooling the system by about 5 %. If the temperature T_h is higher than the temperature T_{sat} , the melt would be undersaturated by $\Delta T_h = T_{\text{sat}} - T_h < 0$ and is ready to melt-with the thin GaAs layer on top of the ridge. After melt-stick is performed in the undersaturated solution for an appropriate time, the sample is moved to the next well with a supersaturated melt for the preferential growth of the current blocking layer.

The samples grown by this scheme are shown in Figures 3.10 and 3.11. In this scheme, in general, the thin GaAs layer on top of the ridge is easily melt-stick. However, the melt-stick may provide a favorable condition for the growth of

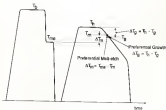


Figure 3: Temperature program for the scheme of preferential melt-etch in undercooled solution followed by preferential growth.

$\Delta T_m = T_m - T_0 < 0$: undercooling for melt-etch of bulk layer,

$\Delta T_0 = T_m - T_0 > 0$: supercooling for growth of melt blocking layer.

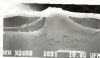


Figure 2 (a) Preferential etching of GaAs layer is underdrifted solution followed by preferential growth of the current blocking layer, underdriftation $\Delta T_{\text{drift}} = -5.5^{\circ}\text{C}$ (cool-down), melt-rich time $t_{\text{m}} = 48$ sec, superdriftation $\Delta T_{\text{drift}} = 5.5^{\circ}\text{C}$ (growth), cooling rate $\beta = 0.7^{\circ}\text{C/min}$.

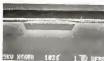


Figure 2-11. Preferential melt-etch of base layer in undersaturated solution followed by preferential growth of the current blocking layer. The current blocking layer was grown over the ridge. undersaturation $\Delta T_0 = -2.5^\circ\text{C}$ (melt-etch), melt-etch time $t_0 = 10$ min, supersaturation $\Delta T_1 = 5.5^\circ\text{C}$ (growth), cooling rate $R = 0.7^\circ\text{C/min}$.



Figure 1-14. In the sample with ferrite, blocking layer grown over the ridge, the I-V curve shows that 10^4 Å typical p-n-p-n structure

the current blocking layer over the ridge, and very often the current blocking layer deposits on top of the ridge as shown in Figure 3.11. Some of the samples have 1-2 current-voltage characteristics shown in Figure 3.12 which is characteristic of a typical p-n-p-n structure. In conclusion, the self-etch of the thin GaAs layer on top of the ridge should be performed after a preferential growth of the current blocking layer.

3.3.4 Preferential Growth Followed by Preferential Self-Etch in Underestimated Relation

In this scheme, first a $n\text{-Ga}_{1-y}\text{Al}_y\text{As}$ current blocking layer is preferentially grown outside the ridge. In this step, a very thin current blocking layer may grow over the ridge. Then, the thin GaAs layer and possibly the very thin current blocking layer on top of the ridge are self-etched in the underestimated self-etch which is prepared by using the temperature program shown in Figure 3.13. The annealing temperature T_a should be adjusted properly so that the underestimation $\Delta T_a (= T_{\text{max}} - T_a = \delta)$ is appropriate.

This scheme will be successful only when the $n\text{-Ga}_{1-y}\text{Al}_y\text{As}$ current blocking layer which is preferentially grown outside the ridge is an effective self-etch mask. In the case geometry, however, even a small self-etch selectivity between $n\text{-Ga}_{1-y}\text{Al}_y\text{As}$ current blocking layer and the GaAs layer is good enough to remove the thin GaAs layer on top of the ridge where the self-etch is easily achievable. Thus, a $n\text{-Ga}_{1-y}\text{Al}_y\text{As}$

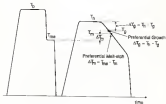


Figure 3.13 Temperature program for the scheme of preferential growth followed by preferential melt-etch in undersaturated solution

$\Delta T_{sup} = T_{sup} - T_0 > 0$: supersaturation for growth
 versus blocking layer.

$\Delta T_{sub} = T_{sub} - T_0 < 0$: undersaturation for
 melt-etch of GaAs layer

layer even with a very low Al concentration ($y = 0.250$) can be an effective wet-etch mask.

The required underetch time Δt_u may depend on the wet-etch mask Al concentration and the wet-etch time t_w . Since the SiGe layer to be wet-etched is very thin (0.3 μm), the relatively short wet-etch time ($t_w = 12$ sec) is reasonable. The temperature drop during the short wet-etch time can be negligible, and thus the underetch time of the mask during the wet-etch process can be assumed constant. Various examples given by this scheme are shown in Figures 3-14, 3-15, and 3-16.

In the sample shown in Figure 3-14(b), the underetch time was too small ($\Delta t_u = +1.5$ sec) and the SiGe layer was not completely removed via the SEM picture, the SiGe layer is usually seen as a bright line. However, in the sample shown in Figure 3-14(c), the SiGe layer was cleanly removed with increased underetch time $\Delta t_u = +2.5$ sec. In general, the current blocking layer becomes thin in the region far from the ridge due to the smaller growth rate. However, as seen in Figure 3-15, the $n\text{-Ge}_{0.2}\text{-pSi}_{0.8}$ current blocking layer even with a relatively low Al concentration ($y = 0.1$) was still intact in the region far from the ridge. The shape of the current blocking layer near the ridge can be also controlled by adjusting the growth time t_g . As shown in Figure 3-16, the current blocking layer becomes flat as the growth time t_g increased. Finally, Figure 3-17 shows the

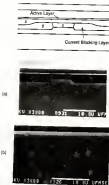


Figure 3.14 Electrodeposition of the current blocking layer followed by preferential multi-step of same layer. (a) Schematic diagram. Electrodeposition, superposition $\Delta V_p = 5.0 \text{ V}$ (growth), multi-step time $t_m = 10 \text{ min}$, scanning rate $s = 0.7 \text{ V/min}$, (b) $\Delta V_p = -1.5 \text{ V}$, $s = 0.30$, $y = 0.30$, $x = 0.30$, (c) $\Delta V_p = -2.0 \text{ V}$, $s = 0.30$, $y = 0.30$, $x = 0.30$.



(a)



(b)

Figure 6. Dendritic growth on the surface blocking layer defined by potential mismatch of DNA layer in undercooled solution, supersaturation $\Delta T_s = 1.0^\circ\text{C}$ (growth), undercooling $\Delta T_u = 1.5^\circ\text{C}$ (melting), melt-cool time $t_c = 10$ sec, cooling rate $\dot{T} = 0.2^\circ\text{C/min}$, $x = 0.15$, $y = 0.15$, $z = 0.15$.
 (a) Growth near the ridges.
 (b) Growth far from the ridges.



(a)



(b)

Figure 3.14 Preferential growth of the current blocking layer followed by preferential etching of this layer. (a) undercoated, electrolyte, superheated $\Delta T_0 = 1.5^\circ\text{C}$ (growth), halt-time time $t_0 = 10$ sec, cooling rate $\beta = 0.1^\circ\text{C/min}$, (b) $\Delta T_0 = -0.5^\circ\text{C}$, $\alpha = 0.15$, $\gamma = 0.10$, $\epsilon = 0.10$, growth time $t_0 = 10$ sec, (c) $\Delta T_0 = -1.5^\circ\text{C}$, $\alpha = 0.10$, $\gamma = 0.10$, $\epsilon = 0.10$, growth time $t_0 = 100$ sec.



Figure 1(a) A typical I-V characteristic for the sample grown by the scheme of preferential growth of the current blocking layer followed by preferential multi-step or undirectional etching.

typical I-V curve for the sample with the GaAs mesa well-etched completely:

3.5 Fabrication Sequence of the Reversed-Ridge-Stripped Finer Structure

In this section, the whole procedure to fabricate the RST structure is summarized. Figure 3.18 shows each growth step of the RST structure.

3.5.1. First Step IPE Growth

The first step growth is performed at temperature of $+450^{\circ}\text{C}$ with a cooling rate of 0.5°C/min . The three layers - a p-GaAs buffer layer ($p = 1 \times 10^{18} \text{ cm}^{-3}$, 1 μm), a p- $\text{Ga}_{0.45}\text{In}_{0.55}\text{As}$ ($p = 1 \times 10^{17} \text{ cm}^{-3}$, 1 μm) layer, and a GaAs (undoped, 0.3 μm) layer - are grown on a (100) oriented p-type GaAs substrate ($p = 1 \times 10^{18} \text{ cm}^{-3}$).

3.5.2. Ridge Formation

After the first step growth, a reversed ridge is formed along the $\langle 11\bar{1} \rangle$ direction as shown in Figure 4.18(a) by using chemical etching in a $\text{NH}_4\text{OH} : \text{H}_2\text{O}_2 : \text{H}_2\text{O} = 30 : 7 : 100$ solution at room temperature. The height and top width of the ridge are about 1.5 μm and 5 μm , respectively. Instead of the reversed ridge, a standard ridge along the $\langle 11\bar{1} \rangle$ direction may be used. However, the reversed ridge has advantages over the standard ridge for the processing required in the next

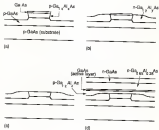


Figure 3-18 The growth procedure of the buried-ridge-stripped pincer GaAs/Al structure.
 (a) Flash stop growth and ridge formation.
 (b) Preferential growth of the narrow blocking layer.
 (c) Preferential etch-back of data layer on top of the ridge.
 (d) Growth of the double heterostructure.

two steps. 1st., preferential growth and preferential etch-back.

3-4-3: Second Step: 1st Growth

In the second step growth, the cooling rate is increased to 1.1°C/min . First, a $n\text{-Ga}_{0.99}\text{Al}_{0.01}\text{As}$ ($\phi = 1.5 \times 10^{17} \text{ cm}^{-3}$, $x = 0.01$) current blocking layer is preferentially grown outside the ridge as shown in Figure 3-18(a). Then, the thin GaAs on top of the ridge is etch-etched in an under-saturated solution ($\text{OH}_2 = -1 \sim -3^{\circ}\text{C}$ depending on the current blocking layer Al mole fraction x) as shown in Figure 3-18(b). After that, the four layer double heterostructure is grown as shown in Figure 3-18(c). The four layers are $p\text{-Ga}_{0.99}\text{Al}_{0.01}\text{As}$ ($\phi = 2 \times 10^{17} \text{ cm}^{-3}$, $0.3 \mu\text{m}$) lower cladding layer, undoped GaAs ($2.25 \sim 0.15 \mu\text{m}$) active layer, $n\text{-Ga}_{0.99}\text{Al}_{0.01}\text{As}$ ($\phi = 2 \times 10^{17} \text{ cm}^{-3}$, $1.5 \mu\text{m}$) upper cladding layer, and the $n\text{-GaAs}$ ($\phi = 2 \times 10^{18} \text{ cm}^{-3}$, $1 \mu\text{m}$) contact layer respectively.

3-4-4: Etching/Growth/Contact

For the $n\text{-electrode}$, 1500 \AA Au-Ge , 100 \AA Ni , and 2000 \AA Au are sequentially deposited on the junction side of the sample by electron beam evaporation.

3-4-5: Lapping

The substrate side of the sample is uniformly lapped until the sample thickness is less than about $100 \mu\text{m}$ (~ 4

will. This step is essential for a good cleavage of the sample.

3.4.4. P-Type Ohmic Contact

For the p-contacts, 200 Å Cr and 2000 Å Au are deposited sequentially on the substrate side by electron beam evaporation.

3.4.5. Anneal

The ohmic materials deposited in step (4) and (6) are annealed at about 450 °C for about 3 min in a 90 % H_2 and 10 % N_2 environment.

3.4.6. Cleaving

The sample is cleaved into individual chips with sawing length of 100 µm.

CHAPTER FOUR

COMPLEX DOMAIN EFFECTIVE INDEX METHOD

4.1- Introduction

The effective index method is one of the most frequently used methods in the analysis of the optical devices such as waveguides and the semiconductor laser diodes [Kane76, Breda71]. The main advantage of the method lies in its simplicity. In the analysis of the most common guides, a very complicated two-dimensional problem is easily handled as two one-dimensional problems in the real domain. However, this real domain effective index method has some limitations. The refractive index is in general a complex number, especially in the semiconductor lasers, and due to their interdependencies, it may not be possible to separately consider the real and imaginary parts of the complex refractive index. Furthermore, either the transverse mode or the lateral mode may not exist in the real domain. For example, in the channelled substrate planar (CSP) lasers [Bred78], the transverse mode in the region outside the channel doesn't have a solution in the real domain, even though real refractive indices (no loss or gain) are assumed. The primary reason is that the modal field outside the channel is not well confined, due to close proximity of the higher index substrate to the active layer, and substrate radiation occurs. Such a leaky mode results in complex

effective index. On the other hand, is lateral leaky mode (anti-guided) structures, which has received considerable attention recently [Kocakli, Hwang, Kwon91]. The lateral mode has always a complex solution.

In this chapter, the conventional real domain effective index method is extended into the complex domain. In the complex domain effective index method, the refractive index is assumed as a complex number due to either gain or loss and the solution of the mode is iteratively searched in the complex domain. As a result, the effect of both the gain and loss is taken into account automatically. Previously, complex modes (by which we mean the modes with complex propagation constant) for solid cavity have been calculated to analyze the DBR structures [Karyn, Dumas] or the anti-guided layer (AGL) structures [Hwang, Chin, Ishii]. However, the effect of the gain may be significantly large to change the structure itself under normal operating conditions. For example, as a result of the active layer gain, an unbounded leaky mode (no physical existence) in solid cavity may become a bounded mode with a non-zero active layer optical confinement [Feng91]. This chapter mainly deals with the development of the complex domain effective index method. This method will be applied to analyze the buried-ridge striped plasmas structure in chapter 5.

4.2. Complex Domain Characteristic Equation

In this section, a very general N-layer characteristic equation is derived in the complex domain. The characteristic equation expressed in the real domain may not be very useful for the analysis of the complex mode structures. The complex domain characteristic equation is derived by using a similar procedure as in the derivation of the real domain characteristic equation, except that the refractive index is treated as a complex number given by either loss or gain. A very general N-layer structure shown in Figure 4.1 is considered. In the structure, the n -th layer is assumed to have thickness d_n ($n = 1, \dots, N-1$) and complex refractive index \hat{n}_n ($n = 1, \dots, N$) defined by

$$\hat{n}_n = n_n + j(\alpha_n - \alpha_n)/\omega \quad (4.12)$$

where $k = 2\pi/\lambda$ is the free space propagation constant and λ is the wavelength, and n_n , α_n , and α_n are real refractive index, loss, and gain in the n th layer, respectively. We assume that the field varies along x direction as

$$\exp(j\omega t - \beta_z z) \quad (4.13)$$

where ω and β_z are the angular frequency and the longitudinal propagation constant, respectively. In semiconductor lasers, in general, the lasing modes have dominantly TE polarization, since the TE mode has lower threshold than the TM mode. For

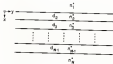


Figure 1.1 A general N-layer structure. The d_j and n_j^x are the thickness and refractive index of the j th layer, respectively.

the TE mode, the transverse electric field $E(x)$ in each layer of the structure of Figure 4-1, can be expressed by [Sak(77)]

$$E(x) = \begin{cases} C_0 \exp(-k_0 x) & (x < 0) \\ C_0 \exp(-k_0 x) \left(\sum_{n=1}^N A_n \right) + & (0 = x_1 = \dots = x_{N-1}) \quad \sum_{n=1}^N A_n + \alpha = \sum_{n=1}^N A_n \\ C_0 \exp(-k_0 x) \left(\sum_{n=1}^N A_n \right) & (x > \sum_{n=1}^N A_n) \end{cases} \quad (4.21)$$

where the n -th layer transverse propagation constant k_n is uniformly defined by

$$k_n = (\epsilon_0 \mu_0)^{-1/2} \sqrt{\epsilon_n^2 - \beta^2} \quad (4.22)$$

For the TE mode, the transverse magnetic field $H(x)$ can be expressed in a similar form as in the equation (4.21). By applying boundary conditions at various interfaces, the following characteristic equation is obtained.

$$\exp(-j k_0 A_0) = \alpha + j\gamma \quad (4.23)$$

$$\text{where } \alpha = \frac{\epsilon_0 \left(\frac{j k_0 A_0 + \tanh(k_0 A_0)}{k_0 A_0} + \frac{j k_0 A_0 - \tanh(k_0 A_0) \tanh(k_0 A_1)}{k_0 A_0 + \tanh(k_0 A_0) \tanh(k_0 A_1)} \right)}{\epsilon_0 \left(\frac{j k_0 A_0 + \tanh(k_0 A_0)}{k_0 A_0} + \frac{j k_0 A_0 - \tanh(k_0 A_0) \tanh(k_0 A_1)}{k_0 A_0 + \tanh(k_0 A_0) \tanh(k_0 A_1)} \right)} \quad (4.24)$$

$$\gamma = \frac{\epsilon_0 \left(\frac{j k_0 A_0 + \tanh(k_0 A_0)}{k_0 A_0} + \frac{j k_0 A_0 - \tanh(k_0 A_0) \tanh(k_0 A_1)}{k_0 A_0 + \tanh(k_0 A_0) \tanh(k_0 A_1)} \right)}{\epsilon_0 \left(\frac{j k_0 A_0 + \tanh(k_0 A_0)}{k_0 A_0} + \frac{j k_0 A_0 - \tanh(k_0 A_0) \tanh(k_0 A_1)}{k_0 A_0 + \tanh(k_0 A_0) \tanh(k_0 A_1)} \right)} \quad (4.25)$$

$$B_1 = \frac{(\epsilon_1 - \epsilon_2)A_1 - \epsilon_2 A_2}{(\epsilon_1 - \epsilon_2)A_1 + \epsilon_2 A_2} + \frac{(\epsilon_2 - \epsilon_3)A_3 + \epsilon_3 A_4 (\epsilon_2 - \epsilon_3)A_2}{(\epsilon_1 - \epsilon_2)A_1 + \epsilon_2 A_2 + (\epsilon_2 - \epsilon_3)A_3 + \epsilon_3 A_4 (\epsilon_2 - \epsilon_3)A_2} \quad (4.8)$$

$$i1 = i2 = \dots, \quad n-2$$

$$B_n = \frac{(\epsilon_n A_n - \epsilon_{n+1} A_{n+1})}{(\epsilon_n A_n + \epsilon_{n+1} A_{n+1})} \quad (4.9)$$

$$B_1 = \frac{(\epsilon_1 A_1 - \epsilon_2 A_2) + (\epsilon_2 A_3 + \epsilon_3 A_4 (\epsilon_2 - \epsilon_3) A_2)}{(\epsilon_1 A_1 + \epsilon_2 A_2) + (\epsilon_2 A_3 + \epsilon_3 A_4 (\epsilon_2 - \epsilon_3) A_2)} \exp(-j\epsilon_2 d_2) \quad (4.10)$$

$$i1 = i2, \quad \dots, \quad n-2$$

$$B_{n-1} = \frac{(\epsilon_{n-1} A_{n-1} - \epsilon_n A_n)}{(\epsilon_{n-1} A_{n-1} + \epsilon_n A_n)} \exp(-j\epsilon_n (d_n - d_{n-1})) \quad (4.11)$$

$$F_0 = \begin{cases} 1 & \text{for TE mode} \\ (1/\epsilon_0)^2 & \text{for TM mode} \end{cases} \quad i1 = i2, \quad \dots, \quad n \quad (4.12)$$

$$\text{Angle} = \gamma z = \begin{cases} \arctan(\gamma/\alpha) & \alpha > 0, \quad \gamma > 0 \\ \arctan(\gamma/\alpha) + \pi & \alpha > 0, \quad \gamma < 0 \\ \arctan(\gamma/\alpha) + 2\pi & \alpha < 0, \quad \gamma > 0 \end{cases} \quad (4.13)$$

In the derivation of the characteristic equation (4.6), the n -th layer was used as a reference layer. The particular form of the characteristic equation is preferred to find a mode which has a peak(s) in the n -th layer. The choice of the reference layer may depend on the structures and the mode types to be found. However, the equation (4.5) has in general multiple solutions, and thus it is not easy to use since a

variables easily hops from one branch to another during mode search process. By taking logarithm derivatives of the exponential functions of the equation (8.11), an inverse form of the characteristic equation

$$k_0 k_z = -\frac{1}{2} \ln(\rho^2 + \eta^2) + \frac{1}{2} \arg(\rho + j\eta) + j\pi \quad (8.14)$$

$$M = 1, 2, 3, \dots$$

is obtained. In equation (8.14), the integer M is not necessarily odd even when k_z the index of layer is larger than three. With fixed α and k_z , the equation (8.14) has a single solution and is preferred over the equation (8.10).

It is noted that the TE polarization in the transverse waveguide is seen as the TM polarization in the lateral waveguide. Thus, in the lateral mode analysis, the characteristic equation for the TE mode would be used. In this case, the transverse parameters k_z and η_z^2 in the equations (8.10)-(8.14) should be replaced by the corresponding lateral parameters.

4.3. Muller Method

Muller method is a very powerful algorithm to find complex roots [Mull68, Mull75]. The method uses a quadratic approximation, based on three points, to the function whose roots are sought. A root of the quadratic approximation is then used as an estimate of the true root, and the process is

repeated iteratively. Let the characteristic function be $f(z)$, whose roots are sought in the complex z -plane, and let z_{k-2} , z_{k-1} , and z_k be three points in the neighborhood of a root. The quadratic approximation $f(z)$, which agrees with $f(z)$ at the given three points, can be expressed by [Sant69]

$$\begin{aligned} f(z) &= f(z_k) + f'(z_k)(z-z_k) + \frac{1}{2}f''(z_k)(z-z_k)^2 \\ &= f(z_k) + a_1(z-z_k) + \frac{1}{2}f''(z_k)(z-z_k)^2 \end{aligned} \quad (8.16)$$

$$\text{where } a_1 = f'(z_k)(z_{k-1}-z_k) + \frac{1}{2}f''(z_k)(z_{k-1}-z_k)(z_{k-2}-z_k) \quad (8.17)$$

$$f'(z_k)(z_k-z_{k-1}) = \frac{f(z_k)(z_k-z_{k-1}) - f(z_{k-1})z_k}{z_k - z_{k-1}} \quad (8.17)$$

$$f''(z_k)(z_k-z_{k-1}) = \frac{f(z_k)(z_k-z_{k-1}) - f(z_{k-1})z_k}{z_k - z_{k-1}} \quad (8.18)$$

Then, the next best estimate of the true root of the $f(z)$ is assumed to be one of the two roots of $f(z)$ and is denoted by z_{k+1} .

$$z_{k+1} = z_k + \frac{-2f(z_k)}{a_1 + b_1} = -2f(z_k) / [f'(z_k)(z_{k-1}-z_k) + \frac{1}{2}f''(z_k)(z_{k-1}-z_k)(z_{k-2}-z_k)] \quad (8.19)$$

In equation (8.19), the sign is usually chosen so that the magnitude of the denominator is as large as possible. This process is repeated with a new set of three points, z_{k-1} , z_k , and z_{k+1} , until the magnitude $|f(z_{k+1})|$ is small enough

Overall flow chart for complex mode search is shown in Figure 4-2.

4.4 Branch specification in the outermost layers

In general, in the case of an x -dimensional polynomial functions, the complex roots are easily found by the Muller method. However, this is not the case for the mode characteristic equation. The difficulty of the Muller method in the complex mode search is often related with the branch specification in Equation (3.4) in the outermost layers, where only one of the two signs of the square root should be chosen. The guide lines for choosing the proper branch are dictated by physical considerations of the modes or the structures [Seki77]. One example of the complex mode structure is found in the region outside the channel of the CDR laser and is shown in Figure 4-3. In this structure, the lower cladding layer (p -Ga_{0.5}As_{0.5}) is not thick enough (poor cladding), and the mode is barely isolated from the substrate with a higher refractive index. As a result, the evanescent tail in the lower cladding layer suffers outward radiation [Sire74]. However, in the upper cladding layer (n -Ga_{0.5}As_{0.5}) which is assumed very thick, the evanescent tail would be significantly damped, before the tail sees the cap layer. These arguments may help to specify the proper branches for the transverse propagation constants, $\kappa_2 = (\kappa_{02})^2 = \beta_2^{1/2}$ and $\kappa_1 = (\kappa_{01})^2 = \beta_1^{1/2}$ in the layer 2 and layer 3 respectively.

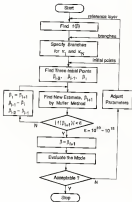


Figure 4.2 The flow chart for attack of the complex mode.

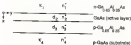


Figure 4-2 An example of the complex mode structure: the lower cladding layer thickness d_2 is relatively small and the mode is not confined.

For the sake of convenience, let α^* be either α_1^* or α_2^* , and similarly let β be either β_1 or β_2 . When the magnitude of the complex refractive index α^* is relatively small (compared to the magnitude of the complex mode index $\beta = \beta/\alpha$ of the mode which is sought), the α^2 would usually lie, depending on the loss in the outermost layer, either in the second (as shown in the Figure 4.4(a)) or the third quadrant of the complex α^2 -plane. In this case, the physical consideration tells that the mode behavior in the outermost layer should be dominated by the exponential decay, as in the layer 1 of the example structure of Figure 4.3. The transverse propagation constant β with larger negative imaginary part describes a field dominated by exponential decay and is named the bounded branch. It is safe to specify the branchcut (which can be specified anywhere mathematically) as far away from the α^2 as possible. In this fashion, the α^2 may not cross the branchcut during search process and α will remain a single valued function. For the bounded branch, the branchcut is specified along the positive real axis of the α^2 -plane and the β with a negative imaginary part is chosen as the proper branch (physical branch) as shown in Figure 4.4(a). The proper branch β with a negative imaginary part will specify an exponentially decaying field as in the layer 1 of the example structure of Figure 4.3. In the analysis of the conventional guided mode structures, the bounded branch should be specified for both the dielectric layers.

Another important branch is the leaky branch which is found useful to describe leaky modes. In the leaky mode structures, the magnitude of the complex refractive index n' is relatively large compared to the magnitude of the complex mode index $n = \beta/k$, at least in one of the two outermost layers. And thus, the β^2 would usually lie, depending on the loss in the outermost layer, in the first or fourth quadrant of the complex β^2 -plane as shown in Figures 4.4(b)-4.4(d). In this case, the physical consideration tells that the mode behavior in the outermost layer should be dominated by the outward power flow (radiation), as in the layer 4 of the example structure of Figure 4.3. The wavevector propagation constant k with a larger positive real part describes a wave which is dominated by outward power flow (propagating outward) and is named the leaky branch. For the leaky branch, the branchcut is specified along the negative real axis of β^2 -plane and the k with a positive real part is chosen as the proper branch as shown in Figures 4.4(b)-4.4(d). The proper branch k with a positive real part will describe a wave propagating outward as in the layer 4 of the example structure of Figure 4.3.

The field described with the leaky branch would be either bounded or unbounded depending on the loss in the outermost layer or the gain in the active layer. In the leaky mode structures, without any optical gain, the power in the guide layer would decrease (due to the optical leakage) as the mode propagates. Similarly, the amount of the leakage itself would decrease at the same rate as the power in the

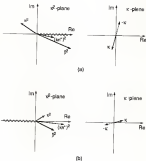


Figure 4.4 Proper branches (a) in the subsonic region, (b) Bounded branch, rounded type, (c) Family unbounded leafy branch.

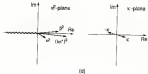
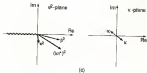


Figure 4.3 Continued
 (a) Passive bounded leaky branch,
 (b) Active bounded leaky branch

guide. However, if the loss in the outermost layer is negligible $(\text{Im}\epsilon')^2$ with small imaginary part) as in the case shown in Figure 4.4(b), the wave propagating outward at a certain angle $(\text{Im}\epsilon')^2$ would not experience significant loss, and the amplitude would not change considerably along the optical path. In this case, the field identified by the proper branch K with a positive imaginary part as specified in Figure 4.4(b), would give in the transverse direction as shown in Figure 4.5(a). However, when the loss in the outermost layer is very high $(\text{Im}\epsilon')^2$ with large imaginary part) as in the case shown in Figure 4.4(c), the wave propagating outward would experience significant loss and would decay more rapidly than the power in the guide. In this case, the field identified by the proper branch K with a negative imaginary part as specified in Figure 4.5(b) would lead to decay exponentially, as shown in Figure 4.5(b). A leaky mode may have net positive mode gain Q with a positive imaginary part, as in the case shown in Figure 4.4(d) when the active layer gain is large enough to overcome the mode loss due to the outward power flow. In this case, the field would be always bounded as shown in Figure 4.5(d), even though no loss is assumed in the outermost layer.

It is noted that for the leaky mode structures the outward power flow is more of a fundamental feature than either the boundedness or unboundedness of the field. If the limit of along the positive real axis as in Figure 4.4(a) is used for the leaky mode structures involving loss contained

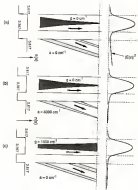


Figure 4.3 Various leaky modes, active layer = $2.4 \mu\text{m}$, cladding layer = $0.3 \mu\text{m}$: (a) Positive refractive index, (b) Positive refractive index, (c) Active refractive index

regarding the boundedness or unboundedness of the field, the k^2 (which would usually lie in the first or fourth quadrant for the leaky type branch) may cross branches very often during the search process. In this case, the complex mode search would fail, since k is not a continuous function along the branches.

In order to thoroughly analyze a complex mode structure, various continuations of the branches should be tested for the two outermost layers. In general, first the bounded branches should be specified for both the outermost layers. In this fashion, the conventional guided type mode will be found first, if the structure supports this type of mode. Otherwise, the search procedure would fail and a different set of branches should be specified (see Figure 8.2). For example, if the structure is asymmetric, we should specify the bounded branch for the outermost layer with smaller magnitude of the refractive index and the leaky branch for the other outermost layer, respectively; if the procedure succeeds, a mode which is bounded on one side and leaky on the other side is found; in this type of mode, in general, inward power flow (i.e. with negative real part) would occur in the outermost layer where the bounded branch is specified, and outward power flow would occur in the other outermost layer. This type of mode is known as the contra-leaky mode (Tadokoro). If the leaky branches are specified for both the outermost layers, leaky modes with outward power flow in both the outermost layers are found; this type of mode is

known as the velocity mode (Tanaka), and is generated in very noisy. If a new mode is found, the mode is evaluated, for example, by plotting the mode profiles. If the mode is not acceptable, appropriate adjustments in the important parameters, such as the substrate layer, thickness, and initial points, are made over the flow chart in Figure 4.17.

4.5 Plane-wave Uniform Approximation of Resonant-Straggles Index Profile

In the complex domain effective index method, most importantly, the refractive index is treated as a complex number either by gain or loss as seen in equation (4.1). Injected carriers confined in the active layer give rise to the optical gain. The active layer gain $g(y)$ is related to the injected current density $J(y)$ (Haller, Starik)

$$g(y) = 45 \frac{J(y)}{d} - 100 \quad (4.20)$$

where the active layer thickness d is in μm , $J(y)$ is in A/cm^2 , and $g(y)$ is in cm^{-1} . In general, the active layer gain g is y -dependent, since the current density is not uniform due to the lateral current spreading. Hoesen et al. [Hoes72] estimated the current density profile $J(y)$ by

$$J(y) = \begin{cases} J_0 & 0 \leq y \leq d/2 \\ J_0/2 + (J_0/2)(1 - y/d) & d/2 \leq y \leq d \end{cases} \quad \begin{matrix} 0 \leq y \leq d/2 \\ d/2 \leq y \leq d \end{matrix} \quad (4.21)$$

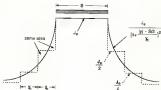


Figure 8.2 A piecewise uniformly approximated current density profile for internal mode analysis.

where W is the current stripe width, $r_0 = (2/100) \sqrt{A_p J_{ed}}^{1/2}$ is the characteristic current spreading length, R_p is the lateral current spreading resistance, and J_0 is the current density under the stripe which is assumed uniform. The optical mode would also experience losses due to scattering, free carrier absorption, and band-gap absorption. In our case, overall losses of 15 cm^{-1} , 7 cm^{-1} , and 1000 cm^{-1} are assumed in the active layer, cladding layer and substrate, respectively [Kurobe, Sakaki]. The gain induced refractive index change, Δn_g , may be included in the real part of the complex refractive index of equation (4-3). Δn_g can be expressed by

$$\Delta n_g = -\frac{1}{2} \frac{(g + 1/20)}{2\pi} \quad (4-12)$$

where g is the line-width enhancement factor, and its assumed value lies between 2 to 3 in GaAs/GaAlAs lasers [Sakaki].

Upon substituting the values for the complex refractive index in each layer, the complex mode index is calculated by solving the transverse mode characteristic equation. In general, the complex effective index would not be uniform in the lateral direction, since the current density J is y -dependent as seen in equation (4-2). The non-uniform current density profile $J(y)$ is often sliced into an appropriate number of sections, and usually a planar

uniform approximation would be made. For example, the two-dimensional piecewise uniform current density profile [10,11,12] shown in Figure 4.4 may be used. By solving the TRANSECT mode characteristic equation in each section of the piecewise uniform current density, a similar piecewise uniform complex transverse effective index profile $N_{\text{eff}}(y) = \beta_{\text{eff}}(y)/k$ is obtained. The lateral mode analysis involving solving the lateral mode characteristic equation determined by the piecewise uniform complex effective index profile $N_{\text{eff}}(y)$:

4.4- Mode gain

In the analysis of the laser, one of the most important step is to calculate the mode gain (modal gain). In the conventional approach, the mode gain is usually estimated by the overlap integral of the gain profile and mode profile. For example, in a standard double heterostructure, the mode gain is estimated by

$$g_m = \frac{\int_{-\infty}^{\infty} g(y) |H(y)|^2 dy}{\int_{-\infty}^{\infty} |H(y)|^2 dy} \quad (4.32)$$

where d is the active layer thickness. When the gain is uniform in the transverse direction in the active layer ($g(y)$

$\approx \beta$ as is usually assumed, the equation (4.21) is simplified to

$$G_0 = \Gamma \beta \quad (4.24)$$

where $\Gamma = \int_0^d \text{Re}(\beta) dz / \int_0^d \text{Re}(\beta) dz$ is the active layer optical confinement factor. More accurately, the mode gain G_0 estimated by equation (4.23) is the transverse mode gain, since it may hold only for modes with infinite width in the potential narrow stripe device, the modes would experience nonuniform gain in the lateral direction, and the mode gain G may be estimated by

$$G = \frac{\int_{-\infty}^{\infty} \int_0^d |\psi(x, y)|^2 |\beta(x, y)|^2 dz dy}{\int_{-\infty}^{\infty} \int_0^d |\psi(x, y)|^2 dz dy} \quad (4.25)$$

However, the overlap integral in equation (4.25) is usually very difficult to evaluate, since the mode profile is not known in the lateral direction. Another problem is that the mode gain is usually overestimated in the laser mode structures, since the overlap integral does not take into

account the structural loss due to such as the optical radiation

In the complex domain effective index method, the transmission mode gain G_0 and mode loss A_0 are simply defined by

$$G_0(\beta) = -A_0(\beta) = 2\text{Im}(\beta_0/\beta) = 2k_0\text{Im}(\beta_0/\beta) \quad (4-24)$$

and is β -dependent. Similarly the overall mode gain G and the mode loss A are defined by

$$G = -A = 2\text{Im}(\beta_p) = 2k_0\text{Im}(\beta_p) \quad (4-25)$$

where β_p is the lateral mode longitudinal propagation constant which is obtained by solving the lateral mode characteristic equation, and $\beta_p = k_p/\alpha$ is the lateral mode effective index.

The transmission mode gain G_0 and mode loss A_0 estimated by both the overlap integral method and the complex domain effective index method are shown in Figure 4-7 and 4-8, respectively. In these figures, Γ_0 is the optical confinement factor in the n -th layer when the lower cladding layer is the structure of Figure 4-1 is thick enough ($d_1 > 1-5 \mu\text{m}$). The structure can be safely assumed as a three layer structure. In the three layer case, the mode gain or loss estimated by the two different methods are relatively in good agreement. In the overlap integral method, the overlap in the central refractive layer is as effective as that in the outer (cladding) layer to contribute to either the mode gain or

mode loss, while in the complex domain effective index method the overlap in the central layer is more effective than that in the outer layer. Thus, the overlap integral method slightly underestimates the mode gain (given by the active layer gain) as shown in Figure 4.7, while slightly overestimates the mode loss (given by the cladding layer loss) as shown in Figure 4.8.

Figure 4.9 shows the mode gain as a function of the lower cladding layer thickness d_2 . The mode gain estimated by overlap integral does not change significantly as the cladding layer thickness decreases. However, the mode gain estimated by the complex domain effective index method drops very rapidly at smaller cladding layer thickness. This higher mode loss at smaller cladding layer thickness is well understood as is the case with surface plasmon coupling (SPLC) since the waveguide structure is very similar to that in Figure 4.1. The reason for the discrepancy of the two methods at small cladding layer thickness is that the overlap integral approach does not take into account the structural loss such as optical leakage. The factor Γ_{122} represents only the gross contribution to the mode gain. α'_2 is the optical confinement factor in the active layer (layer #1). Thus, the overlap integral method is good only in the conventional guided mode regime where the structural loss is negligible. However, in the complex domain effective index method, both the structural loss and the absorption loss are

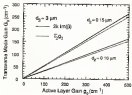


Figure 4.1 Transverse mode gain estimated by both overlap integral method and coupled-mode effective index method.

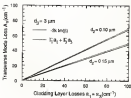


FIGURE 4.4 Transverse mode loss estimated by both varying integral method and coupled domain effective index method.

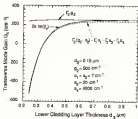


Figure 4.5 Transverse mode gain as a function of the lower cladding layer thickness d_3 .

approximately taken into account, since the refractive index is assumed as a complex number.

In this sense, the gain estimated by equation (4.24) and (4.27) are net mode gain. The overlap integral approach can also be extended to estimate the net mode gain by including the effect of the optical radiation and absorption. The optical radiation would die out in the substrate layers to eventually, due to the band to band absorption. Thus, the net mode gain may be estimated by overlap integral as $\Gamma_1 Q \Gamma_2 - \alpha_0 = \Gamma_1 \alpha_1 - \Gamma_2 \alpha_2 - \Gamma_3 \alpha_3$ α_0 is the optical confinement factor in the n -th layer. The net mode gain estimated by the overlap integral is reasonably in good agreement with that estimated by the complex domain effective index method as compared in Figure 4.4. However, one of the problems in the overlap integral approach is that the mode profiles should be estimated by an independent method. Sometimes the overlap integral would not be available as in the case of the uncoupled leaky modes, even though the mode profiles are known.

Figure 4.10 shows the variations of the resonant mode gain G as a function of the piezoelectric active layer gain whose piezoelectric value is $q_{31} = 45 \frac{\text{dyne}}{\text{cm}^2} = 180$ for an example of the SHF amplifier. The threshold is achieved when the net mode gain is equal to the output mirror loss, $\frac{1}{2} \ln \left(\frac{1}{R_1 R_2} \right)$ (1 and 2 are the length and the intensity reflectivity of the cavity

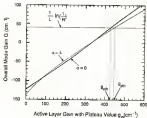


Figure 8.60 Overall mode gain as a function of the active layer gain in the DBEP structure, $d_1 = 0.1 \mu\text{m}$, $d_2 = 0.3 \mu\text{m}$, $\alpha = 0.25$, $\gamma = 0.35$, $\kappa = 0.35$.

respectively. The threshold current density at the current injection stripe, J_{th} , is determined by [Rose73]

$$J_{th} = J_{sat}(1 + \gamma_{sp}/\beta) = \frac{qV_{th}n_{sp}}{A} (1 + \gamma_{sp}/\beta) \quad (4.24)$$

where V_{th} is the threshold active layer gain as shown in Figure 4.18.

4.5. Structural Loss Estimation

In order to estimate the external differential efficiency, η_{ed} , the gross mode loss should be estimated in addition to the net mode gain (striped mirror loss). The gross mode loss (resulting from such as the optical leakage, absorption, and scattering) in the mode loss determined by the structure itself. In the complex domain effective index method, the structural loss is estimated approximately as the mode loss determined with no active layer gain, since the mode gain is relatively linear with the active layer mode gain as shown in Figure 4.18. In reality, the relationship between mode gain G and the active layer gain g_a is not strictly linear, since the added gain (complex refractive index) changes the structure itself. The nonlinear relationship between mode gain G and the active layer gain g_a is more severe when we assume the gain induced refractive index change Δn . Thus, in general, the structural loss (scavity loss) at threshold is estimated by linear

extrapolation between two points, i.e., $q_0 = q_{th}$ and $q_0 = 0$, by using the extrapolation, the cavity loss R_0 at threshold is estimated by

$$R_0 = 2\alpha_{th}R_{th} - \frac{1}{2} \ln\left(\frac{1}{Q_0}\right) \quad (4.20)$$

where α_{th} is the slope of the mode gain vs. active layer gain curve at threshold as shown in Figure 4.8 and is given by

$$\alpha_{th} = \left(\frac{\partial G}{\partial g_a}\right)_{g_a=g_{th}} \quad \text{at } q_0 = q_{th} \quad (4.21)$$

In equation (4.20), the derivative $\frac{\partial G}{\partial g_a}$ is taken with fixed g_a so that the structure does not change during the slope evaluation. The external differential efficiency η_{ext} is then expressed by

$$\eta_{ext} = \frac{\text{mirror loss}}{\text{mode loss} + \text{mirror loss}} = \frac{\frac{1}{2} \ln\left(\frac{1}{Q_0}\right)}{R_0 + \frac{1}{2} \ln\left(\frac{1}{Q_0}\right)} \quad (4.22)$$

In our previous work [LandHe], the cavity loss R_0 was divided into two parts, i.e., the mode loss due to the lateral optical leakage and mode loss due to the internal absorption. In the practical narrow stripe devices, the mode loss due to optical leakage plays a dominant role compared to

the mode loss due to the absorption, since the lateral optical leakage increases very rapidly as the stripe width a decreases [14-15a]. It is noted that the lateral optical leakage is relatively large even in the positive index step structures as a result of the gain induced refractive index change Δn_g . The detailed calculations remain for the near future will be presented in chapter 5.

4.4 Summary and Conclusion

The complex domain effective index method has been developed by extending the conventional real domain effective index method into the complex domain in straight forward fashion by assuming complex effective indices given by either gain or loss. The complex domain effective index method is very powerful for the analysis of both the conventional guided mode structures and the leaky mode structures. A very general N -layer complex domain characteristic equation was derived for both the transverse mode and the lateral mode and solved by the the Muller method.

Two types of branches, i.e., the bounded branch and the leaky branch were introduced to describe the field in the outermost layers. The leaky branch is extremely useful to describe the field in the outermost layer where optical radiation takes place. It is noted that the mode search with the conventional branch specification (by either the bounded type and unbounded type branches) often fails in the leaky mode structures.

In the leaky mode structures, the mode gain is often overestimated by the conventional overlap integral, since the effect of the structural loss is not taken into account. However, in the complex domain effective index method, the effect of the structural loss is automatically included as well as the effects of both loss and gain.

CHAPTER FIVE

ANALYSIS OF THE BURIED-RIDGE-STRIPED PLASMA STRUCTURE

5.1 Introduction

In this chapter, the buried-ridge striped plasma (BRSP) structure is analyzed by using the complex domain effective index method developed in chapter 4. A structure with either a negative or a complex effective index step can easily be analyzed by using the complex domain effective index method. The BRSP structure can incorporate virtually all of the effective index steps, such as complex, negative, and positive index steps, since the k_z value fraction of the current blocking layer can be variedly almost independently from that of the buried ridge which carries a part of the lower cladding layer. A schematic diagram of the BRSP structure which shows important parameters is represented in Figure 5.1.

5.2 Mode Analysis

The BRSP structure can be divided laterally into two regions, i.e., the region inside the buried-ridge-stripe and the region outside the stripe. The stripe region can be analyzed as a four layer structure, since the mode, in general, is well confined in the buried-ridge layer. However, in the region outside the stripe, the transverse mode may not be confined enough in the current blocking layer depending on



Figure 5.1 A schematic diagram of the MBE structure. The x , y , and z are Al mole fractions in the buried-ridge, current blocking, and lower cladding layer, respectively, and the d_1 , d_2 , d_3 , and d_4 are the thicknesses of the buried-ridge, current blocking, and lower cladding layer respectively. If not specified otherwise, we assume $d_1 = 8.10 \mu\text{m}$, $d_2 = 1.10 \mu\text{m}$, $d_3 = 1.0 \mu\text{m}$, $d_4 = 0.5 \mu\text{m}$, $x = 0.20$, upper cladding layer Al mole fraction = 0.10, and wave length $\lambda = 0.88 \mu\text{m}$.

the current blocking layer refractive index n_f and thickness d_f . In this case, the effect of the substrate can not be neglected any more, and therefore, the region outside the stripe should be analyzed as a five layer structure. Previously, a four layer structure was analyzed in the study of the etched substrate planar HEBI structure [Kang98, Hwang01]. In general, the analysis of a five layer structure is much more complicated than that of the four layer structure.

Indeed, the current blocking layer refractive index n_f is an important parameter that determines the modal behavior outside the stripe. The index n_f can be related to the RI ratio fraction r as shown in Figure 3.2. The curve was obtained by interpolating the measured data by Kang et al. [Kang98]. Figure 3.3 shows the complex mode indices as a function of the current blocking layer refractive index n_f for three modes ($M = 0, 1, 2$) found outside the stripe. For the sake of convenience, the range of the current blocking layer refractive index n_f is divided approximately into three cases, i.e., lower refractive index case ($n_f < 3.42$), median refractive index case ($3.42 < n_f < 3.50$), and higher refractive index case ($n_f > 3.50$). The mode profiles for the three modes ($M = 0, 1, 2$) in the three separate cases are shown in Figures 3.4-3.6, respectively.

In the lower current blocking layer refractive index case ($n_f < 3.42$), the $M = 0$ mode has a relatively large active layer optical confinement, since the mode is well

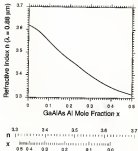


Figure 3.2 The relationship between refractive index, n and Al mole fraction, x for GaAlAs layer at wavelength $\lambda = 0.88 \mu\text{m}$ (Case 54).

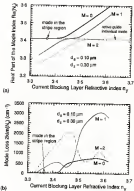


Figure 5.3 The complex mode index as a function of the current blocking layer refractive index n_y . (a) Real part, (b) imaginary part

damped in the current blocking layer (negligible substrate radiation) as shown in Figures 3.4(a), however, the $M = 1, 2$ modes are largely confined in the current blocking layer as shown in Figures 3.4(b) and 3.4(c). For these modes, the effect of the substrate cannot be neglected and, in general, significant radiation occurs into the substrate with the higher refractive index. The oscillatory behavior of the field profiles as shown in Figures 3.4(b) and 3.4(c) implies power radiation. As a result, the transverse mode loss for the $M = 1$ and $M = 2$ modes is relatively large (complex mode index with a large imaginary part) as shown in Figure 3.3(b).

It is noted that, as shown in Figure 3.3, the mode in the stripe region (marked by a small circle (c)) is located in the $M = 0$ branch. In the lower current blocking layer refractive index case ($n_2 < 3.42$), the $M = 0$ mode has a very similar mode profile as in the stripe region while the other modes are very much distorted (Figures 3.4(a)-(c)). In this case, the stripe mode would couple dominantly to the $M = 0$ mode compared to the higher modes ($M = 1, 2$) [Taheri, Okamoto]. Therefore, in the lower current blocking layer refractive index case, the $M = 0$ mode is a principal mode and the higher modes can be neglected in the analysis.

In the medium current blocking layer refractive index case ($3.42 < n_2 < 3.5$), even the $M = 0$ mode has significant mode loss ($\alpha_s > 400 \text{ cm}^{-1}$) as shown in Figure 3.3(b), since the mode is not damped in the current blocking layer as shown in Figure 3.3(a) leading to a significant substrate radiation.

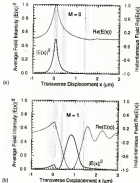


Figure 5.4 Mode profiles in the lower current blocking layer (refractive index $n_2 = 3.388$, $\gamma = 0.20$). (a) $M = 0$ mode, (b) $M = 1$ mode.

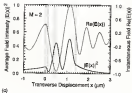


Figure 3.4 Downloaded
 60- M = 2 mode

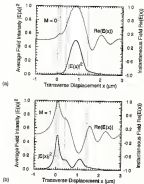


Figure 5.3 Mode profiles in the surface current blocking layer (refractive index $n_2 = 3.480$, $y = 2.5\lambda$)
 (a) $M = 0$ mode, (b) $M = 1$ mode.

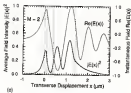


Figure 5-5 Continued.
 (a) $M=2$ mode.

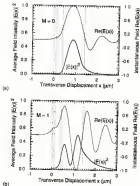


Figure 8.8 Mode profiles in the higher current blocking layer reflexive case ($\lambda_0 = 2.54\mu\text{m}$, $y = 0.10$)
 (a) $M = 0$ mode, (b) $M = 1$ mode.

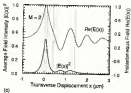


Figure 3.4 COLL: Lenses
(a) $m=2$ mode.

In this region, the active guide individual mode lies is closer to the $M = 1$ mode than to the other modes ($M = 2$), as shown in Figure 3.3(a). Thus, the stripe mode will have a similar mode profile with the $M = 1$ mode compared to the other modes. However, in this case, the $M = 2$ mode may not be neglected in the analysis, since the $M = 2$ mode with relatively large active layer optical confinement as shown in Figure 3.3(b) have a considerable overlap with the stripe mode.

In the higher current blocking layer refractive index case ($n_b > 3.5$), the $M = 2$ mode shown in Figure 3.3(c) has a large active layer optical confinement and would have significant overlap with the stripe mode. On the other hand, both the $M = 0$ mode and $M = 1$ mode are mostly confined in the current blocking layer with a negligible overlap with the stripe mode. Thus, in the higher current blocking layer refractive index case, the $M = 2$ mode is the principal mode and the other two modes ($M = 0, 1$) can be neglected in the analysis.

3.3 Effective Index Map

In the WPP structure, the built-in effective index step can be controlled by varying the refractive index of the current blocking layer. The built-in effective index step Δn is defined by

$$\Delta n = n_a - n_b \quad (3.1)$$

where n_a and n_b are the effective indices of the principal modes at each cavity in the regions inside and outside the

buried-ridge stripe, respectively. This built-in effective index step is very important to control the lateral mode on a narrow stripe geometry.

In the lower current blocking layer refractive index case ($n_y < 3.42$), the effective index step can have either a positive and a negative value depending on the n_y . If the n_y is larger than the buried-ridge layer refractive index n_x , the effective index step becomes negative. On the other hand, if the n_y is smaller than the buried ridge layer refractive index n_x , the effective index step becomes positive. The effective index steps calculated in the lower current blocking layer refractive index case are shown in Figures 3.7 and 3.8.

In the higher current blocking layer refractive index case ($n_y > 3.4$), the effective index step has complex values since the principal mode ($m = 0$) in the region outside the stripe has complex effective index with a large imaginary part. The complex effective index step (both the real part and the imaginary part) in the higher current blocking layer refractive index case is calculated as shown in Figure 3.9.

The complex effective index step can also be achieved in the middle current blocking layer refractive index case ($3.42 < n_y < 3.50$) as well, since all the modes outside the stripe have complex effective index with large imaginary part. However, the effective index step may not be simply defined by equation 3.1, since the principal mode can not be clearly defined in the region outside the stripe as explained in

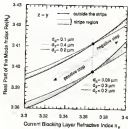


Figure 3.7 Effective index map variation as a function of the current blocking layer refractive index n_B ($n_c = n_B$, $z = y$).

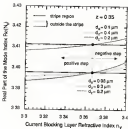


Figure 5.3 Effective index step variation as a function of the current blocking layer refractive index n_f ($n_1 = 3.388$, $\alpha = 0.25$).

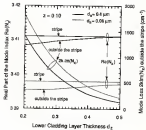


Figure 3.3 Effective index step variation as a function of the central blocking layer thickness d_2 in μm , $n_1 = 3.44$, $p = 0.101$.

section 3.3. In order to analyze more accurately, all the modes outside the stripe should be considered. For example, by the approaches used in the previous study of the separated multi-striated layer (MSL) structure [Suzuki, Chikari].

The effective index step for cold cavity would change as a result of the gain induced refractive index change Δn_g . Figures 3.10, 3.11, and 3.12 show the calculated complex effective index profile at threshold for the positive, the negative, and the complex step structures, respectively. Since in the position as the negative step structures where the substrate reflection is virtually eliminated outside the stripe, the imaginary part of the effective index has a relatively small step between inside and outside the stripe as shown in Figure 3.10 and 3.11. In this case, the real part of the effective index step is primarily responsible for the lateral mode stabilization. However, in the complex step structures with significant substrate reflection outside the stripe, the imaginary part of the effective index has a very large step between inside and outside the stripe as shown in Figure 3.12 compared to the case of either the positive or the negative step structures. Thus, in the complex step structures, the lateral mode is relatively stable even though gain induced refractive index change Δn_g affects the real part of the effective index step [Suzuki, Chikari]. Similar stable modes have been observed in other complex index step structures [Kuroki, Hayashi, Suzuki, Sano, Miyajima].

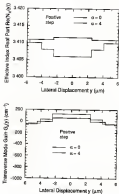


Figure 3.12 The complex effective index distribution at threshold ($\gamma = \alpha = 0.48$, positive step)

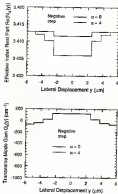


Figure 5.11 The complex effective index distribution as threshold ($\gamma = \alpha = 0.30$, negative steps).

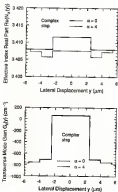


Figure 5.12 The complex effective index distribution at threshold ($\gamma = 0.05$, complex step).

Another important point is that, in the positive step structure, the positive step in the real part of the effective index may shift to the negative step as shown in Figure 3.18(a), as a result of the gain induced refractive index change Δn_2 . However, in the negative step structure (Figure 3.11(a)), the Δn_2 actually increases the size of the negative step. Thus, in the negative step structure, the optical characteristics, such as the threshold and the mode loss may not be very sensitive to the Δn_2 when compared with the positive step structure.

3.4. Experimental Results

In this section, experimental results are presented. Figure 3.13 shows the light output vs. drive current characteristics and the far field patterns for both the negative step structure (N-MSR) and the positive step structure (P-MSR). The negative step structure suffers a large mode loss due to the internal optical leakage, and thus the threshold current for the negative step structure is usually larger than that of the positive step structure as shown in Figure 3.13. In general, the negative step structures exhibit very unstable lateral modes compared to the positive step structures, even though unstable lateral modes are often observed in the positive step structure as well. The unstable lateral modes with relatively large stripe width ($> 4\mu\text{m}$) both in the negative step structure and the positive step structure are expected since the imaginary part

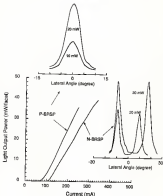


Figure 5.13 The optimal characteristics of both the negative step (N-BSPF) and positive step (P-BSPF) VC structures.

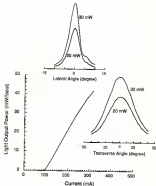


Figure 5.14 The optical characteristics of the complex step ACB device.

of the complex effective index has a relatively small step between inside and outside the ridge compared to that of the complex step structure. As expected, in the negative step structure, the two-lobed far field pattern shown in Figure 3-13 is often observed [Sag177].

Figure 3-14 shows the typical light output vs drive current characteristic and the far field pattern for the complex step RBSF structure. The typical threshold current of the complex step structure is larger than that of the positive step structure but smaller than that of the negative step structure. In general, stable internal modes are observed more often in the complex step structures than either in the positive step structure and the negative step structure. The stable internal mode in the complex step structure is due to the large imaginary step of the complex effective index [Kuroda, Iwabe]. Figures 3-15-3-17 show the variations of both the structural loss α_s and the external differential efficiency η_{ext} as a function of the ridge width.

3.4. Blazed-ridge

The blazed-ridge striped planar (BRSP) structure has been demonstrated to have a very wide range of effective index steps, i.e., the positive step, the negative step, and the complex step. As expected, two-lobed far field pattern was observed in the negative step structure while single-lobed far field pattern was observed either in the positive step and the complex step structures.

In the conventional DBR type laser with complex index step, coherent beating has been observed in the small area over the channel direction [Fukuda, Tokuda]. However, in the complex step DBR structure, the $\text{Ga}_{1-y}\text{Al}_y\text{As}$ current blocking layer with enhanced band-edge absorption as a result of the increased bandgap isolates the active layer further away from the substrate where the substrate radiation would involve absorption and beating. Furthermore, in the DBR structure, the longer optical radiation path from the active region to the substrate would make the beating effect less diffused over a wider area.

As seen in Figures 5.10-5.12, the measured values of extracted differential efficiency η_{ext} are relatively smaller than the theoretical values which seem to be more reasonable. In the positive step structures, the η_{ext} decreases significantly as we assume the gain induced refractive index change $\Delta n_2 = -\alpha_{\text{sp}}(190/\lambda^2)$ as shown in Figure 5.13. The positive index step shifts to a negative step as a result of the Δn_2 (Figure 5.13(a)), thus the structure loss R_2 increases leading to a decreased η_{ext} . The air-width broadening factor α may be geometry dependent [Ozida, Inaba], and the assumed value $\alpha = 4$ seems too high. However, in both the negative step and the complex step structure, the η_{ext} is less sensitive to the Δn_2 . The relatively low measured η_{ext} is the one of the indications that the device quality is not very good. The reasons for the poor device quality may be found in the lack of the growth

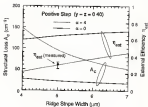


Figure 9.15 The structural loss A_0 and the external efficiency η_{ext} as a function of the stripe width (positive step)

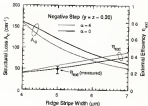


Figure 5.13 The structural loss A_s and the external efficiency η_{ext} as a function of the stripe width (negative step).

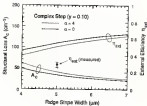


Figure 8.17 The structural loss A_s and the external efficiency η_{ext} as a function of the slope width (complex step).

refinement due to the primitive IFT system and beam design, low quality substrate (etch pit density $\sim 10000 \text{ cm}^{-2}$), and the lack of clean room facility.

It is speculated that the DBF structure may prove to be of importance in the realization of high quality linear array lasers. Previously, linear array lasers have utilized either the DBF type structure [Hotehi] or the BB type structure [Hakiki] as shown in Figures 1.4 and 1.5, respectively. In the DBF type linear array lasers, the significant substrate radiation loss between elements is to maintain the lateral coupling similarly to the leaky mode coupled BB type linear array lasers as shown in Figure 1.5, the discontinuous active layer results in a significant diffraction loss between elements (backward guide mechanism) leading to a minimized lateral coupling. However, in the DBF type linear array lasers as schematically shown in Figure 1.18, the optical loss is negligible between elements and leads to strong transverse coupling which is essential for a stable array mode operation. The DBF type linear array lasers would have the flexibility to control the effective index step with some advantages over the leaky-mode coupled array laser by Hotehi et. al. [Hotehi] which requires regrowth on a Gaq qdls pds layer.

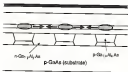


Figure 3.13 Schematic diagram of the leaky mode coupled SHF type linear taper

CHAPTER SIX SEPARATED LARGE OPTICAL CAVITY LASERS

6.1 Introduction

There is considerable interest in increasing the output power of the semiconductor diode lasers. The increased output power is desirable in several areas, e.g., optical recording, laser printing, space communication, and the pumping of solid state lasers [Kallist]. One approach to produce large output power is to increase the mode size in the transverse direction [Meadell, Fiquett] by using, for example, a thin active layer (TAL) or the large optical cavity (LOC). In this chapter, a novel separated large optical cavity (SLOC) structure [Meadell, Kallist] shown in Figure 6.1(a) is proposed and tested. It permits the increase in the effective transverse mode size and thereby the output power. The modal behavior is explained by the coupling of several modes under gain.

In the conventional LOC structures [Kallist], the carrier confinement in the active layer may become poor, especially at high injection levels, due to the reduced energy barrier between the active layer and the LOC layer with relatively small bandgap. However, in the SLOC structure, a relatively thin 10×10^3 Å p-type 10^{18} cm⁻³ layer separates the active and LOC layer providing sufficient barrier for the confinement of n-type electrons. The active layer carrier confinement is

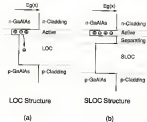


FIGURE 8.2 Carrier confinement in the active layer:
 (a) Large optical cavity structure,
 (b) Separated large optical cavity structure.

Both the conventional SAG structure and the SLOC structure are compared in Figure 4.2.

4.2 Mode Analysis

The first layer SLOC structure may be considered as a set of strongly coupled waveguides consisting of the active guide and the SLOC guide. As the two guides become closer to each other, individual modes from each guide are perturbed by the presence of the other guide. The perturbed modes are the normal modes of the composite structure. Figure 4.3 shows the variation of the mode indices as a function of the SLOC layer refractive index.

In general, as the SLOC layer refractive index increases, the number of modes increases. As an example, when the SLOC layer refractive index is 3.08, the entire composite structure supports the three modes ($M = 3$, i. e.) shown in Figure 4.4. In this case, the $M = 2$ and $M = 1$ modes are essentially the perturbed individual SLOC-guide modes and are mostly confined to the SLOC layer. However, the $M = 3$ mode which is closer to the active guide (individual mode line) is associated with the individual active guide mode, and therefore, has higher active layer optical confinement (lower threshold) compared to the other two modes. This situation will change as the refractive index of the SLOC layer changes. For example, when the SLOC layer refractive index is increased to 3.45, the $M = 1$ mode is closer to the active guide (individual mode line) and will have the higher

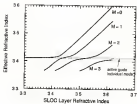


Figure 8-3 The calculated mode indices as a function of the SLDG layer refractive index

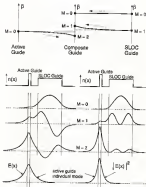


Figure 6-4 An example of normal modes in the SLOC structure (SLOC layer refractive index = 3.45).

active layer optical confinement (lower threshold) compared to the other two modes ($m = 0, 1$).

4.2 Experiment

The SLOC scheme was applied to two different geometries: the oxide-defined stripe structure and the buried-ridge striped planar (BSP) structure. The oxide-defined stripe SLOC structure (Figure 4.11a) was prepared by sequentially growing seven layers using MBE on a (100) oriented p-type substrate (n-doped, $p = 1 \times 10^{18} \text{ cm}^{-3}$). The seven layers were a p-GaAs ($p = 1 \times 10^{18} \text{ cm}^{-3}$, 2 μm) buffer layer, a p-GaAs spike spike ($p = 2 \times 10^{17} \text{ cm}^{-3}$, 1.5 μm) SLOC-cladding layer, a p-Ba_{0.5}Sb_{0.5} spike spike ($p = 2 \times 10^{17} \text{ cm}^{-3}$, 1 μm) SLOC layer, a p-GaAs spike spike ($p = 2 \times 10^{17} \text{ cm}^{-3}$, 0.5 μm) separating layer, a GaAs (undoped, 2.5 μm) active layer, a n-GaAs spike spike ($n = 2 \times 10^{17} \text{ cm}^{-3}$, 1.5 μm) upper cladding layer, and a n-GaAs ($n = 2 \times 10^{18} \text{ cm}^{-3}$, 1 μm) contact layer sequentially. After a 0.5 μm thick oxide film was deposited on the n-side, a 10 μm wide contact stripe was opened in the oxide. In the case of the BSP SLOC structure (Figure 4.11b), the growth procedure is basically same as in the regular BSP structures, except that the SLOC layer is additionally grown. Metal contacts of Au-Ge/Ni/Au and Cr/Au were formed on the both samples for n and p electrodes, respectively. The samples were then cleaved into individual chips with cavity length of 200 μm . The chips were tested using pulsed excitation (pulse width = 0.5 ps).

For the sake of comparison, we fabricated non-SLOC lasers, i.e., a standard oxide-defined stripe double heterostructure laser and a standard DBR laser. The dimensions and growth parameters of the non-SLOC lasers are same as those of the corresponding SLOC lasers respectively, except for the omission of SLOC guides. Figure 4-5 and 4-6 show both the light output vs. current characteristics and the transverse far field patterns for the oxide-defined striped SLOC structure and the DBR SLOC structure, respectively. In the both SLOC and non-SLOC oxide-defined stripe lasers, the threshold currents are relatively high as shown in Figure 4-5, because of the severe lateral current spreading in the relatively thick ($2.5 \mu\text{m}$) n-type cladding and contact layers. The threshold current of the SLOC oxide-defined stripe laser is higher than that of the non-SLOC oxide-defined stripe laser. However, the maximum available output power of the SLOC laser is about twice that of the non-SLOC laser. Similarly, as shown in Figure 4-6, the maximum output power of the SLOC DBR laser is about twice that of the non-SLOC DBR laser.

4.4. Gain-Induced Transverse Effects

The increased output of the SLOC lasers with accompanied increase in the threshold is one to be understood in terms of the increase in the effective transverse mode size. It is believed that, in the SLOC structure, the high gain or gain-induced nonlinearity in the active layer causes coupling

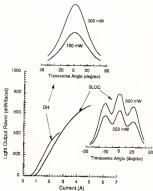


Figure 4.5 The light output vs. current characteristic and the transverse angle field patterns in the GaInAsSb stripe SLOC structure.

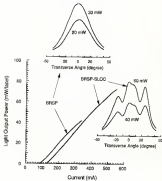


Figure 6.4 The light output vs. current characteristics and the transverse electric field pattern in the BRSP-SLOC structure.

among the normal modes. This is expected since, in general, the power orthogonality in a guided wave structure fails in cases with either gain or loss [Chia80]. In a previous study on the twin-guide laser by Suenaga et. al, an external guide was incorporated to couple out the laser beam [Suen89].

The mode index of the individual single mode active guide ($M = 0$) is 3.41184, while the mode indices of the individual SLOC guides are 3.48181 and 3.42281 for $M = 2$ mode and $M = 1$ mode, respectively. It is seen that the individual active guide mode ($M = 0$) index is closer to that of the first order mode ($M = 1$) of the individual SLOC guide. The interaction of the two individual modes results in normal modes $M = 1$ and 2 of the composite structure. The calculated mode indices of the composite structure for $M = 0, 1$, and 2 are 3.48175, 3.42986, and 3.42178, respectively. If coupling occurs indeed, it is more likely that the active guide mode of the composite structure ($M = 0$) couples primarily with the $M = 1$ mode rather than with the $M = 2$ mode, since the $M = 2$ mode with significantly larger mode index has a negligible overlap with the active guide ($M = 0$) mode as seen from Figure 4-3.

The mode coupling between normal modes may be verified by measurement of the transverse mode for fluid patterns. Figures 4-3 and 4-4 also show the measured transverse for fluid patterns. In general, the SLOC structures show multimodes for fluid patterns, while the non-SLOC structures show single lobes for fluid patterns as expected. Since it is

believed that the coupling occurs primarily between axial modes $M = 1$ and $M = 2$, the measured transverse far field patterns is simulated by varying the power ratio P_1/P_2 ($P_2 =$ power in the $M = 2$ mode). Figures 8-15(a) show the calculated transverse far field patterns for $M = 1$ and $M = 2$ modes. The shape of the estimated patterns for wide-defined stripe SLOC structures tends to simulate the measured patterns, for example, when the mode power ratio is assumed to $P_1/P_2 = 0.1/0.7$ as shown in Figure 8-15(b). It is noted that the actual shape of the measured transverse far field patterns varies somewhat, although not significantly, from chip to chip, the estimated shape is consistently observed in almost every case.

The output power may not be increased significantly, if only the active guide mode ($M = 2$) with the largest active layer optical confinement is excited. The relative mode size which is calculated with unit peak amplitude in active layers of the $M = 2$ mode is only 1.15 times larger than that of the active guide individual mode of the non-SLOC structure and therefore, unless the maximum output power in SLOC structures is not achievable without power coupling to the SLOC guide.

8-5 Conclusion

In conclusion, the reported large optical cavity (SLOC) scheme is demonstrated to effectively increase the transverse mode size, and thereby, increases the maximum output power

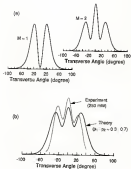


Figure 6.7 Calculated transverse far field patterns in the EBC structure
 (a) Normal modes $M=1$ and $M=2$,
 (b) Combined modes, $p_1, p_2 = 0.5, 0.7$.

above twice that of the SLOC laser. It is shown that the high gain in the active layer seems to cause coupling between normal modes of the composite structure consisting of the active guide and SLOC guide. It is further demonstrated that the complicated far-field profile can be understood by superposition of the normal modes. However, the analysis given here is far from complete. A quantitative analysis is necessary to understand as to how exactly the gain couples the normal modes of the system. This understanding will enable us to optimize the SLOC structure and to increase the maximum output power as well as improve the transverse far field pattern. The SLOC structure is expected to find applications in areas where the beam quality is not critical, e.g., pumping of solid state lasers.

CHAPTER SEVEN

(SUMMARY AND RECOMMENDATION)

7.1. Summary

Both a novel buried-ridge-striped passive (BRSP) structure and a novel suspended large optical cavity (SLOC) structure were proposed, fabricated, analyzed, and tested.

The growth of the BRSP structure was performed by using a novel two-step liquid phase epitaxy (LPE) scheme that involves preferential growth and melt-back. The structure can incorporate a wide range of effective index steps (positive, negative, and periodic), since Al mole fraction in the current blocking layer can be varied from that of the buried-ridge which becomes a part of the lower cladding. In the BRSP structure, the regrowth problem in the second step LPE is minimized, since only the small area of a GaAs in the side wall of the ridge is exposed to air during the etching process to form the ridge. The air-exposed GaAs in the side wall doesn't impede the regrowth seriously (Tuck²⁴).

One of the most important steps in the growth process is the preferential melt-back of the thin GaAs on top of the ridge. In the BRSP structure, the GaAs to be melt-etched is located in an area with convex topography where the melt would be less superheated and thus the melt-back can be performed in a melt with relatively small undercoolation ($\Delta T = -1 \sim -3^\circ\text{C}$). Therefore even a very low Al mole fraction (x

A 0.1 μ m oxide layer with a slightly smaller melt-stick rate compared to a 1 μ m layer can be used as a melt-stick mask. However, in the melt-sticked laser striped (MSLS) structures [Hata85] in which a similar melt-stick scheme was used, the melt-stick should be performed into a relatively deep (2 μ m) channel where the melt would be more superheated due to the increased conductivity. Thus, in the MSLS structures, the melt-stick is performed in a melt with relatively large undercooling ($\Delta T \sim -3^\circ\text{C}$) probably for a relatively long time. Therefore only a large Al melt fraction ($\phi > 0.42$) oxide layer with a very small melt-stick rate can be used as a melt-stick mask. One problem with the MSLS structure is that the melt-in effective index step is very much filled with only a large Al melt fraction melt-stick mask. The refractive index of the melt-stick mask is the most important parameter to determine the effective index in the region outside the stripe.

In order to analyze the MSLS structure, the conventional real domain effective index method was extended into the complex domain. A general N-layer characteristic equation was derived in the complex domain and the equation was solved by using the Muller method [Good80]. The boundary specification in the outermost layer is an essential part in the complex mode search. The conventional bounded branch is useful only for guided mode which is bounded in the bulk outermost layers. A new branch named the leaky branch was introduced to describe the fluid leakage bounded or unbounded in leaky mode.

STRUCTURES. The leaky mode field in the outermost layer is either bounded or unbounded depending on the loss in the outermost layer as the gain in the guide layer.

For the lateral mode analysis, a seven section piecewise uniform approximation was used for the current density j_y as approximated by SOMERS (1982) . In the complex domain effective index method, the mode gain is simply related to the imaginary part of the complex mode index. The mode gain estimated by the conventional overlap integral method is just the gross mode gain and falls in leaky mode structures, since the structural loss such as the optical leakage is not taken into account.

The analysis at threshold shows that both in the positive step structures and the negative step structures, the imaginary part of the effective index exhibits a relatively small step between inside and outside the ridge. Thus, in this case, the lateral mode stabilization is primarily achieved by only the real part of the effective index step. However, in the complex step structure, the imaginary part of the effective index has a very large step between the stripe and outside the stripe region compared to the case either in the positive or the negative step structures. As a result, in the complex step structure, the lateral mode is relatively stable even though the gain induced refractive index change Δn_g affects the real part of the effective index step.

Lastly, in a novel separated stripe optical cavity (SSOC) structure, the maximum output power was about twice that of

the standard two-SLQ structure as a result of the increase in the effective transverse mode size. In general, the orthogonality of the normal modes fails in a guide with coupled refractive index in the SLQ structure. The high gain in the active layer causes coupling between the active guide mode and the SLQ guide mode thereby effectively increasing the transverse mode size. The measured far field patterns were predicted by a linear combination of the normal modes.

7.8 Recommendations for Further Study

There are many areas which need further study. Most important among them are:

Refinement of the MLQ structure design

It is very important to control the thickness of the layers, most importantly the active layer and the lower cladding layer, since these thicknesses are directly related to the magnitude of the effective index of the structure. For a reasonably large effective index step, the lower cladding layer thickness should be less than 0.5 μm and the active layer thickness should be less than 0.1 μm . The active layer thickness is also very important to determine both the threshold and the transverse mode size. In general, as double heterostructure, the thinner active layer provides a lower threshold and an increased mode size.

In order to control the layer thickness, the growth parameters such as the cooling rate, the supersaturation, the seed thickness, and the growth time should be adjusted properly. The cooling rate used in the second stage LPE was 0.7 °C/min. We have found later in the experiment that the cooling rate can be reduced below 0.5 °C/min without a serious growth of the current blocking layer over the top of the ridge. In general, the layer thickness can be controlled more accurately with a reduced cooling rate.

For the sake of completion, some modifications of the LPE system may be necessary to facilitate easier fabrication of the structure. It is very important to purge the chamber as fast as possible to minimize the material oxidation, for example either by attaching a vacuum pump to the system or by significantly increasing the H_2 flow rate (currently the maximum H_2 flow rate is about 50 cc/min due to the diffusion-limited operation of the hydrogen purifier). A glove box may be helpful to minimize the contamination or the oxidation of the materials during the loading process. Our very simple boat design needs to be modified so that the current materials, especially the Al, can be loaded separately to minimize the oxidation of the Al oxide into the well.

Device Characterization

A significant amount of work is needed for device characterization. The device was tested using the pulsed excitation (pulse width = 0.3 msec). A laser green-coupled LED

better condition will reduce the threshold current and increase the efficiency, and the device may be mounted on a heat sink for continuous wave (CW) operation. The device characteristics, such as the reliability, the lifetime, the modulation speed, and the linewidth would be better tested under the condition of CW operation.

DBR-Type Linear Array Laser

The DBR structure is speculated to have a greater potential for linear array applications. Both the negative step and the positive step linear array geometry may be developed. The minimized coupling loss between elements would help obtain very stable array modes.

Analysis and Optimization of the MQW Structure

A quantitative analysis is necessary to understand as to how exactly the gain couples the various modes of the system. This understanding will enable us to optimize the MQW structure and to increase the maximum output power as well as improve the transverse far field pattern.

REFERENCES

- [Ack184] G. E. Ackley, "High-power ridge longitudinal wave operation of bulk channel substrate wave guide (PCHW) lasers," *Electron. Lett.*, vol. 18, pp. 100-101, June 1982.
- [Ack185] G. E. Ackley and R. M. Sapsinawa, "High-power leaky-mode multiple-wave lasers," *Appl. Phys. Lett.*, vol. 38, no. 15-16, July 1981.
- [Amara8] M. Amara, "Rigorous waveguiding analysis of the superlattice multilayer laser-geometry laser," *IEEE J. Quantum Electron.*, vol. 20, pp. 1893-1904, Oct. 1984.
- [Bata76] D. Bates, "Planar and inverted-ridge GaAs waveguide lasers: Device characterization and studies of liquid phase epitaxy growth," Ph.D. dissertation, Univ. of California, Berkeley, Dec. 1976.
- [Bata78] D. Bates, "Optimal cavity design for low-threshold, low-loss-density operation of double-heterojunction diode lasers," *Appl. Phys. Lett.*, vol. 33, pp. 93-95, July 1978.
- [Bata81] D. Bates, "Continuous double-heterojunction AlGaAs diode lasers: structure and spectroscopic characterization," *IEEE J. Quantum Electron.*, vol. 27, pp. 2395-2403, Dec. 1981.
- [Bata82] D. Bates, "Laser diodes are power-packed," *IEEE Spectrum*, June 1982.
- [Bata83] D. Bates and J. E. Conaway, "High-power phase-locked arrays of index-guided diode lasers," *Appl. Phys. Lett.*, vol. 43, pp. 1878-1879, Dec. 1983.
- [Bata85] D. Bates, P. Papadakis, L. J. Mawst, T. J. Smith, and G. Petrosyan, "Diffraction-limited Ga-phasem-mode operation from uniform array of antipodes with reduced intersubband loss," *Electron. Lett.*, vol. 21, pp. 1087-1089, Sep. 1985.
- [Bata86] Bates, D. J. Mawst, P. Papadakis, G. Petrosyan, and T. J. Smith, "High-power, diffraction-limited-beam operation from phase-locked diode-laser arrays of closely spaced "leaky" waveguide antipodes," *Appl. Phys. Lett.*, vol. 49, pp. 686-688, Aug. 1986.

- [Moti63] J. R. Motier and S. Jovan, "Mode Characteristics of Nonlinear double-heterostructure and large-optical-signal laser structures," *IEEE J. Quantum Electron.*, vol. QE-9, pp. 552-561, June 1983.
- [Pue62] J. Puse, "The effective index method and its application to semiconductor lasers," *IEEE J. Quantum Electron.*, vol. QE-8, pp. 1082-1087, July 1982.
- [Cas64] E. C. Casp, D. P. Sheil, and R. B. Fienish, "Refractive index of $\text{Al}_x\text{Ga}_{1-x}\text{As}$ between 0.3 and 1.8 μm ," *Appl. Phys. Lett.*, vol. 24, pp. 42-45, Jan. 1974.
- [Chia82] S. M. Chiao and R. J. Epino, "Calculation of separated multiple-layer stripe geometry laser modes," *IEEE J. Quantum Electron.*, vol. QE-18, pp. 104-109, June 1982.
- [Gee68] G. G. Goss and G. Hoss, *Elementary Numerical Analysis*. New York: McGraw-Hill, 1968.
- [Coo67] D. C. Cook and F. E. Nash, "Self-induced guiding and asymmetric output from AlGa lasers," *J. Appl. Phys.*, vol. 38, pp. 1470-1472, Apr. 1975.
- [Hop66] R. W. Hopmann and S. Corpa, "Leaky modes in active three-layer slab waveguides," *IRE Proc.*, vol. 177, pp. 124-126, Nov. 1966.
- [Kra68] S. A. Kraus, J. R. Mullen, and V. J. Rhee, "Lateral optical confinement of channel-substrate-coupled lasers with GaAs/AlGaAs substrates," *IEEE J. Quantum Electron.*, vol. QE-14, pp. 737-745, May 1968.
- [Pue64] J. Puselet, "Study of twin anti-guiding active slabs," *Opt. Soc. Am.*, vol. 5, pp. 141-171, Nov. 1964.
- [Rig67] L. Rigueux, "GaAs double-heterostructure injection lasers with lateral optical and current confinement," Ph.D. dissertation, Univ. of California, Berkeley, Dec. 1979.
- [Rig68] L. Rigueux, "High-power semiconductor lasers," Chap. 8 in "Handbook of solid-state lasers", ed by P. E. Chen, Marcel Dekker, New York, 1967.
- [Hol68] R. Holstein, M. Ehrenberg, S. A. Hinkel, and J. E. Rether, *Appl. Phys. Lett.*, vol. 13, pp. 510-517, Oct. 1968.

- [Kaw65] K. Kawada, M. Ueda, K. Shimizu, H. Kuro, F. Sato, T. Sakakura, K. Yoshikawa, K. Itoh, G. Kato and T. Yamashita, "A 0.1 μ m DB laser with buried twin ridge substrate structure," 1985 J. Quantum Electronics., vol. QJ-31, pp. 422-428, June 1985.
- [Kaw82] T. Kawanabe, H. Kipuchi, S. Yamamoto, K. Sasaki, K. Terao, and T. Nakano, "Highly reliable and mode stabilized operation in V-channelled substrate laser stripe lasers on p-GaAs substrates emitting in the visible wavelength region," J. Appl. Phys., vol. 53, pp. 7231-7234, Nov. 1982.
- [Kaw84] T. Kawanabe, "Heterostructure lasers," 1984 Trans. Electron. Dev., vol. ED-31, pp. 1439-1442, Nov. 1984.
- [Kip80] T. Kawanabe, K. S. Panish, F. W. Fog, and K. Suzuki, "Injection lasers which operate at room temperature," Appl. Phys. Lett., vol. 37, pp. 109-111, Aug. 1980.
- [Kor62] C. E. Kory, "Theory of the linewidth of semiconductor lasers," 1962 J. Quantum Electronics., vol. QJ-18, pp. 239-244, Feb. 1962.
- [Loh81] K. Itoh, K. Shimizu, K. Takagi, T. Fujimura, and M. Takemura, "Separated multilayer-layer stripe-groove buried DB laser," 1981 J. Quantum Electronics., vol. QJ-27, pp. 1224-1234, July 1981.
- [Maj77] T. Fujimura, K. Itoh, K. Sakai, and K. Ito, "Lowy-mode buried-heterostructure AlGaAs injection lasers," Appl. Phys. Lett., vol. 30, pp. 570-571, June 1977.
- [Mey72] R. Kennard and R. Selman, "Properties and applications of III-V compound films deposited by liquid phase epitaxy," Technical Report, RCA Lab., Princeton, New Jersey, 1972.
- [Mey78] T. Kawanabe, H. Kawanabe, K. Aiki, and J. Kanda, "Channelled-substrate-planar structure AlGaAs DB lasers: An analytical waveplane study," Appl. Opt., vol. 17, pp. 3244-3247, Oct. 1978.
- [Lee87a] S. J. Lee, L. Figueroa, and R. V. Ramamoorthy, "Lowy-grooved channelled substrate planar DB laser with reduced substrate modulation and heating," 1987 J. Quantum Electronics., vol. QJ-33, pp. 1432-1444, July 1987.
- [Lee87b] S. J. Lee, R. V. Ramamoorthy, P. E. Barry, L. Figueroa, and J. E. Kim, "Separated large optical cavity

GaInAs/GaAs diode lasers," IEEE/LEOS Annual Meeting, 1991, B. Orlando, Florida, Oct. 1991.

- [Lee91a] S. J. Lee, S. V. Ramasekany, P. B. Key, and L. Figueroa, "Buried-ridge striped planar GaInAs/GaAs diode lasers with wide range of effective index step," Appl. Phys. Lett., vol. 58, pp. 899-901, Feb. 1990.
- [Lee91b] S. J. Lee, S. V. Ramasekany, P. B. Key, and L. Figueroa, "Normal-mode coupled impinged large optical cavity GaInAs/GaAs diode lasers," to be submitted to Appl. Phys. Lett., May 1991.
- [Lee91c] S. J. Lee, L. Figueroa, and S. V. Ramasekany, "Variations of linewidth enhancement factor and linewidth as a function of laser geometry in AlGaInAs lasers," IEEE J. Quantum Electron., QJ-27, pp. 485-495, May 1991.
- [Lopez88] R. A. Lopez, "DPE of buried heterostructure laser devices," Prog. Cryot. Growth and Charact., vol. 11, pp. 215-241, 1988.
- [Lopez91] R. A. Lopez, R. E. Schumaker, C. E. Kuecy, and P. B. Merritt, "Scaling effects on relaxation frequency in LPE growth and of AlGaInAs DB lasers," J. Appl. Phys., vol. 70, pp. 5552-5557, Sep. 1991.
- [Maro84] E. Maro, C. E. Kuecy, and G. Faschi, "Relation between normal-mode and coupled-mode analysis of parallel waveguides," IEEE J. Quantum Electron., vol. QE-30, pp. 1217-1219, Dec. 1984.
- [Maw91] L. J. Maw, C. Key, T.-J. Roth, G. Petrosian, and J. J. Yang, "Diffraction-coupled, phase-locked arrays of self-aligned, quantum-well lasers grown by metalorganic chemical vapor deposition," Electron. Lett., vol. 27, pp. 948-949, July 1991.
- [Maw91a] L. J. Maw, L. Hsieh, T. J. Roth, W. H. Dimock, E. Peterson, R. Janssen, J. E. Nilsen, and J. J. Yang, "Phase-locked array of self-aligned lasers with nonlinear optical filter," Electron. Lett., vol. 27, pp. 945-946, Mar 1991.
- [Maw91b] L. J. Maw, A. Occhipinti, C. A. Deschinski, R. A. Marshall, and J. J. Yang, "Complementary well-aligned laser by metalorganic chemical vapor deposition," Electron. Lett., vol. 27, pp. 940-941, Sep 1991.

- [Galic77] B. Galic, B. Kono, S. Kanada, S. Shikata, and S. Kono, "A highly reliable CW operation of 100 mW GaAs buried GaIn ridge substrate lasers with non-absorbing mirrors," *IEEE J. Quantum Electron.*, vol. QE-23, pp. 1420-1424, June 1987.
- [Kawai87] Y. Kawai and S. Tada, "Low threshold operation of a GaAlAs/GaAs distributed feedback laser with double channel planar buried heterostructure," *Appl. Phys. Lett.*, vol. 49, pp. 1145-1147, Nov. 1986.
- [Kawai87] S. Kawai, S. Nojima, K. Minomura, S. Syono, S. Kameoka, and S. Nakayama, "Edge waveguide AlGaAs/GaAs distributed feedback lasers," *IEEE J. Quantum Electron.*, vol. QE-23, pp. 108-113, Feb. 1987.
- [Kono74] T. Kono, "Strip loaded film waveguide," *Bell Syst. Tech. J.*, vol. 53, pp. 617-620, Apr. 1974.
- [Galic87] B. Galic and J. Kono, "Linewidth broadening factor in semiconductor lasers - an overview," *IEEE J. Quantum Electron.*, vol. QE-23, pp. 9-25, Jan. 1987.
- [Galic88] B. Galic and S. Ito, "Buried-heterostructure AlGaAs lasers," *IEEE J. Quantum Electron.*, vol. QE-24, pp. 282-288, Feb. 1988.
- [Smith75] R. B. Smith and G. L. Mitchell, "Calculation of complex propagating modes in arbitrary, planar-layered, complex dielectric structures," *OE Technical Rep. no. 104*, Ohio Washington, Seattle, Dec. 1975.
- [Galic78] B. Galic, "Calculated spectral dependence of gain in excited GaAs," *J. Appl. Phys.*, vol. 49, pp. 5382-5385, Dec. 1978.
- [Galic78] B. Galic, B. T. Padden, G. L. Sedgman, "Calculated radiation losses in GaAs heterostructure lasers," *IEEE J. Quantum Electron.*, vol. QE-13, 171-182, Mar. 1978.
- [Galic79] B. Galic, S. Kanada, and S. Nagashi, "Integrated GaIn-ridge AlGaAs laser with multi-heterostructure," *IEEE J. Quantum Electron.*, vol. QE-15, pp. 857-868, July 1979.
- [Tani88] T. Tani and F. Y. Wu, "Variation of leaky waves and their excitation along multilayered structures," *IEEE J. Quantum Electron.*, vol. QE-24, pp. 541-551, Apr. 1988.

- [Tien79] F. H. Tien and R. Ulrich, "Theory of pulse-file coupler and thin film light guides," *J. Opt. Soc. Am.*, vol. 69, pp. 1323-1337, Dec. 1979.
- [Todor68] S. Todoroki, "Influence of lateral heating on current-optical output power characteristics in $\text{Ga}_{1-x}\text{Al}_x\text{As}$ lasers," *J Appl Phys Lett.*, vol. 13, pp. 81-83, July 1968.
- [Todor69] S. Todoroki, M. Sawai, and S. Aiki, "Temperature distribution along the striped active region in high-power GaAs-AlAs visible lasers," *J Appl Phys.*, vol. 40, pp. 1229-1232, Aug. 1969.
- [Toda74] T. Tetsuda, "Liquid-phase epitaxial growth of $\text{Ga}_{1-x}\text{Al}_x\text{As}$ on the side and top surfaces of air exposed $\text{Ga}_{1-x}\text{Al}_x\text{As}$," *Appl. Phys. Lett.*, vol. 22, pp. 427-429, June 1973.
- [Wall69] R. Wallenstein and P. Fomenko, "High power, CW single frequency, THz, GaAs laser pumped Nd:YAG laser," *Electron Lett.*, vol. 5, pp. 1284-1286, Aug. 1969.
- [Wata80] A. Watanabe, T. Yamada, K. Inanaka, S. Kurikawa, Y. Sawai, and S. Todoroki, "AlGaAs/GaAs well-etched laser stripe laser diode with self-aligned structure," *Appl. Phys. Lett.*, vol. 48, pp. 1222-1224, June 1985.
- [Yama82] G. Yamamoto, M. Nishiki, T. Koyama, M. Mizumachi, S. Terao, and T. Aikawa, "High optical power CW operation in visible spectral range by window V-channelled substrate laser stripe lasers," *Appl Phys. Lett.*, vol. 42, pp. 458-459, March 1983.
- [Yang85] J. J. Yang, C. S. Hong, J. Wines, and L. Pinerova, "High-power single longitudinal mode operation of inverted channelled AlGaAs power lasers," *J. Appl. Phys.*, vol. 58, pp. 1440-1442, Dec. 1985.
- [Yone73] S. Yoneda, I. Sakuma, K. Kodasaki, T. Kamejima, M. Sano, and Y. Hamachi, "GaAs-Al_{0.25}Ga_{0.75}As double heterostructure planar stripe laser," *Japan J. Appl. Phys.*, vol. 12, pp. 1265-1272, Oct. 1973.
- [Yone84] M. Yoneda, T. Yano, and T. Shinkawa, "CW optical power from AlGaAs double heterostructure lasers," *Japan J. Appl. Phys.*, vol. 23, pp. 2362-2363, Dec. 1984.

BIOGRAPHICAL SKETCH

Seon Joo Lee was born in Seoul, Korea in 1938. He received the B.S. degree in electronics engineering from the Seoul National University and the M.S. degree in electrical engineering from the Korea Advanced Institute of Science and Technology in 1960 and in 1961, respectively.

From March 1961 to August 1963, he was with the Agency for Defense Development, Seoul, Korea, where he worked on digital system design. In December 1963, he joined the Photonics Research Laboratory at the University of Florida, Gainesville. He was involved in research on the coupling mode (couple mode) analysis and novel semiconductor laser design and fabrication using liquid phase epitaxy.

I certify that I have read this study and that in my opinion it conforms to acceptable standards of scholarly presentation and is fully adequate, in scope and quality, as a dissertation for the degree of Doctor of Philosophy.



Russ V. Sammons, Chairman
Professor of Electrical Engineering

I certify that I have read this study and that in my opinion it conforms to acceptable standards of scholarly presentation and is fully adequate, in scope and quality, as a dissertation for the degree of Doctor of Philosophy.



Robert L. Gray
Professor of Electrical Engineering

I certify that I have read this study and that in my opinion it conforms to acceptable standards of scholarly presentation and is fully adequate, in scope and quality, as a dissertation for the degree of Doctor of Philosophy.



Thomas J. Mc
Professor of Electrical Engineering

I certify that I have read this study and that in my opinion it conforms to acceptable standards of scholarly presentation and is fully adequate, in scope and quality, as a dissertation for the degree of Doctor of Philosophy.



Raymond J. McNamee
Associate Professor of
Electrical Engineering

I certify that I have read this study and that in my opinion it conforms to acceptable standards of scholarly presentation and is fully competent, in scope and quality, as a dissertation for the degree of Doctor of Philosophy.


John C. O'Connell
Associate Professor of
Chemical Engineering

This dissertation was submitted to the Graduate Faculty of the College of Engineering and to the Graduate School and was accepted as partial fulfillment of the requirements for the degree of Doctor of Philosophy.

May 1960


p. William R. Phillips
Dean, College of Engineering

Edw. H. Lombard
Dean, Graduate School